Accelerating the clock: Interconnected speedup of energetic and molecular dynamics during aging in cultured human cells

Authors: Gabriel Sturm[1,2], Natalia Bobba-Alves[1], Robert A. Tumasian III[3], Jeremy Michelson[1], Luigi Ferrucci[4], Christopher P. Kempes[5,*] & Martin Picard[1,6,7,*]

1 Department of Psychiatry, Division of Behavioral Medicine, Columbia University Irving Medical Center, New York, NY, United States
2 Department of Biophysics and Biochemistry, University of California, San Francisco, CA, United States
3 Department of Biostatistics, Mailman School of Public Health, Columbia University, New York, NY, United States
4 Intramural Research Program of the National Institute on Aging, NIH, Baltimore, MD, United States
5 Santa Fe Institute, Santa Fe, NM, United States
6 Department of Neurology, H. Houston Merritt Center, Columbia Translational Neuroscience Initiative, Columbia University Irving Medical Center, New York, NY, United States
7 New York State Psychiatric Institute, New York, NY, United States

* *Correspondence*: ckempes@gmail.com, martin.picard@columbia.edu

The allometric theory of metabolism predicts that the rate of biological aging is proportional to an organism's size and, consequently, its metabolic rate (MR) and partitioning of energy resources between growth and maintenance processes. Here we test this hypothesis in humans by generating longitudinal, multi-modal signatures of aging in primary human fibroblasts. Relative to metabolic rates in the human body, isolated cells exhibit similar MR but markedly elevated growth rates indicating a shift of finite energetic resources away from molecular maintenance and repair processes. Accordingly, per-cell division, isolated cells display reduced lifespan marked by accelerated telomere shortening and increased rate of DNA methylation aging. Moreover, despite a marked reduction in division rate towards the end of life, mass-specific MR increases exponentially, reflecting hypermetabolism. We develop a theoretical-mathematical model that accounts for a partitioning of energetic costs between growth and maintenance, the potential origins of decreased lifespan *in vitro*, and hypermetabolism with advancing cellular age. Moreover, we define genome-wide molecular rescaling factors that confirm and quantify the systematic acceleration of molecular aging kinetics in cultured fibroblasts. We use this approach to show how metabolic and pharmacological manipulations that increase or decrease MR predictably accelerate or decelerate the rates of biological aging. The interconnected speedup of molecular dynamics with growth and energetic rates in human cells has important theoretical and clinical implications for aging biology.

INTRODUCTION

Recent progress has been made to uncover the fundamental mechanisms of aging using quantitative molecular signatures (Wiley and Campisi 2021; López-Otín et al. 2013). These signatures include telomere length, DNA methylation, and cytokine secretion, each with the ability to track the rate of biological aging in human bodies and cultured cells (Horvath 2013; Sayed et al. 2021; Belsky et al. 2022; A. A. Johnson et al. 2020). However, much remains to be uncovered about the connection between aging mechanisms occurring at the organismal level and those at the isolated cellular level. Current models of aging have yet to explain why different biological systems age at different rates and what fundamentally constrains the timescales of lifespan (Rando and Wyss-Coray 2021).

To understand fundamental mechanisms of aging we need contexts in which the timescales can be radically manipulated. There are two dominant ways to consider vastly different timescales. The first is using comparative biology, where across diverse species of mammals many rates and timescales vary by several orders of magnitude. The second is through *in vitro* manipulation of cultured cells where biological rates can be dramatically adjusted. For example, it is well-known that compared to whole organisms, isolated proliferating cells undergo replicative senescence (Hayflick and Moorhead 1964) and exhibit shortened lifespan, meaning that replicating cells maintain a self-sustaining system over months, whereas cells in the body from which they are derived can self-sustain over several decades. Whether this absolute difference is an artifact of replication or reflects fundamentally different timescales between *in vitro* and *in vivo* remains unclear. Here we integrate the comparative approach and *in vitro* experimental approach to examine processes and concepts surrounding biological aging.

Considering the comparative perspective, much of the variation in mammalian physiology can be explained by body size. Scaling laws relating body mass to metabolic rate, organism growth, and lifespan are among the most universal quantitative patterns in biology. These patterns are found in all major taxonomic groups from prokaryotes to metazoans, although with some exceptions (e.g., birds and domesticated dogs) (G. West 2018; J. H. Brown et al. 2004; DeLong et al. 2010; Kempes, Dutkiewicz, and Follows 2012; Hatton et al. 2019). These cross-species scaling relationships can often be connected with fundamental mechanisms and tradeoffs which over evolutionary time are optimized for efficiency (Kempes, Koehl, and West 2019). For example, the nonlinear relationship between metabolic rate and body size has been connected with fundamental transport limitations of vascular systems (G. B.

West, Brown, and Enquist 1997; Geoffrey B. West, Brown, and Enquist 1999; G. West 2018). Within this same framework, the metabolic argument for aging is that smaller mammals have greater vascular delivery to cells which leads to higher cellular metabolic rates, which in turn, is proposed to lead to faster rates of various damage processes and aging (Geoffrey B. West, Woodruff, and Brown 2002; G. West 2018; Hou 2013). This evidence supports the rate of living hypothesis (i.e., animals with faster metabolic rates age faster) and matches longstanding observations indicating that the lifespan of mammals systematically increases with body size following a power law relationship (Speakman 2005b; Schmidt-Nielsen and Knut 1984; Economos 1980). A key concept in this work is that lifespan depends on several factors, most notably, lifespan will decrease if cellular metabolic rates increases, or if more energy is dedicated to biosynthesis relative to repair (**Box 1**). Larger mammals tend to have lower metabolic rates per cell (unit mass) and lower biosynthesis rates all of which is consistent with their longer lifespans. This cross-species perspective suggests that cellular lifespans can be adjusted either by increasing a cell's metabolic rate, or by holding metabolic rates constant and inducing an increase in biosynthesis, which under a fixed budget requires a decrease in repair processes.

Other cross-species work has focused on the connection between somatic mutation rate (Cagan et al. 2022) or telomere dynamics and lifespan (Whittemore et al. 2019). While initial telomere length does not significantly correlate with how long species live, the *rate* of telomere shortening is systematically higher for smaller mammals with higher metabolic rates, leading to an earlier time at which the critical telomere length is reached and cellular viability decreases (Whittemore et al. 2019). At the cellular level, these data are consistent with documented energetic connections with cellular aging (Wiley and Campisi 2021), and further supported by recent evidence that rate of aging is actively modulated by metabolic cooperation and metabolite exchange between cells (López-Otín et al. 2016; Correia-Melo et al. 2022). However, it is important to note that caveats do exist within particular species (Speakman 2005a), where domesticated dogs show the opposite trends of lifespan and body size (Masoro and Austad 2011), which could be due to their unusual evolutionary trajectory.

Fundamentally, the above arguments are about the rate at which different processes (i.e., genomic, epigenomic, metabolic) occur within cells as connected with the whole organism. It is important to note that the metabolic and telomeric perspectives are not inconsistent with one another, because both rates could change in tandem with overall body size, or one could change in response to the other. More generally, it is known that development in different organisms can be viewed as the rescaling of a universal curve (G. B. West, Brown, and Enquist

2001) and recently these ideas have been borne out in detailed molecular studies. For example, the rate of protein synthesis is higher in isolated fibroblasts from species with smaller body weights, and inversely related to animal lifespans (Swovick et al. 2021). And relatedly, anatomical segmentation clocks follow the same developmental sequences but at different rates in different sized mammals (faster in smaller species) (Matsuda et al. 2020).

These cross-species perspectives provide us with a set of testable hypotheses and mechanisms that can be interrogated within-species, in humans. This is achievable using *in vitro* tissue cultures where parallel, longitudinal measurements and manipulations of the rates of metabolism and aging are feasible (Sturm et al. 2019). Here we use the framework of metabolic theory to test the hypothesis that cells isolated from the human body and aged in culture should rescale as if they were a smaller organism and correspondingly show a higher metabolic rate and accelerated rate of aging (Geoffrey B. West, Woodruff, and Brown 2002). More specifically, here we show that: i) a variety of cellular rates and aging markers, including telomere shortening, are rescaled in the same way as growth rates which is consistent with cross-species perspectives on energetic partitioning between growth and repair assuming similar metabolic rates (**Box 1**) ; ii) late-stage *in vitro* cells undergo radical metabolic transition consistent with metabolic features of senescence, including cellular signaling and related processes not related to growth, referred to here as “maintenance”; iii) it is possible to modulate the rates of aging directly through experimental manipulations that shift the balance of energy expenditure between growth and maintenance, and affect metabolic rate consistent with cross-species expectations; and iv) relationships between cell size and metabolic rate of cultured cells are predicted by cross-species scaling relationships. A key strength of our approach is that it relies on direct multi-omic measures of molecular dynamics across the entire life course of a population of cells, rather than on punctual comparisons of specific cellular states (e.g., replicative state vs senescence). Our work is of broad importance because it supports the notion that the rates of aging can be altered in a single species by manipulating metabolic rates.

RESULTS

Expectations from allometric theories

Living organisms resist entropy and sustain life over extended periods of time by consuming energy. The allometric theory of metabolism focuses on energy as a driver of a variety of interconnected physiology (G. West 2018). More specifically, this theory considers which aspects of metabolism and physiology vary across organisms of different size and makes predictions that are relevant to aging at both the whole-organism and single-cell level. For example, for each minute of life, a mouse expends ~25 times more energy per gram of body weight than an elephant does, and lives on average 1/25 (2-3 years) the lifespan of the elephant (Rolfe and Brown 1997; Speakman 2005b). Here we outline three interconnected observations or hypotheses extrapolated from allometric rescaling that occurs when human cells are isolated (i.e., biopsied) and placed in culture **(Box 1; Figure 1A-D)**: i) Within the body, all cells behave as an interdependent, large-scale collective bound by rules and rates specific to the organism (Levin 2021). In contrast, isolating cells away from the organism and placing them in non-confluent cultures in which cells exist as independent entities dramatically increases the growth rate of organisms (**Figure 1A**). Consequently, experimentally manipulating metabolic rate should control the rate of cellular aging (**Figure 1B**) ii) Given that isolated cells maintain approximately the same metabolic rate as they would have in the adult human body, this implies a decrease in allocation of energy to repair purposes which should correspondingly decrease lifespan (**Figure 1C**). Partial support for this hypothesis has previously been provided (Geoffrey B. West, Woodruff, and Brown 2002; Davies 1961). iii) As cultured cells age and decrease in size, their mass-specific metabolic rate should proportionally increase (**Figure 1D**). Box 1 highlights the theoretical-mathematical models underlying these predictions. Here, interspecies trends in metabolic rate and metabolic partitioning are used to predict time-dependent changes in the metabolic rate of human cells during isolation *in vitro*.

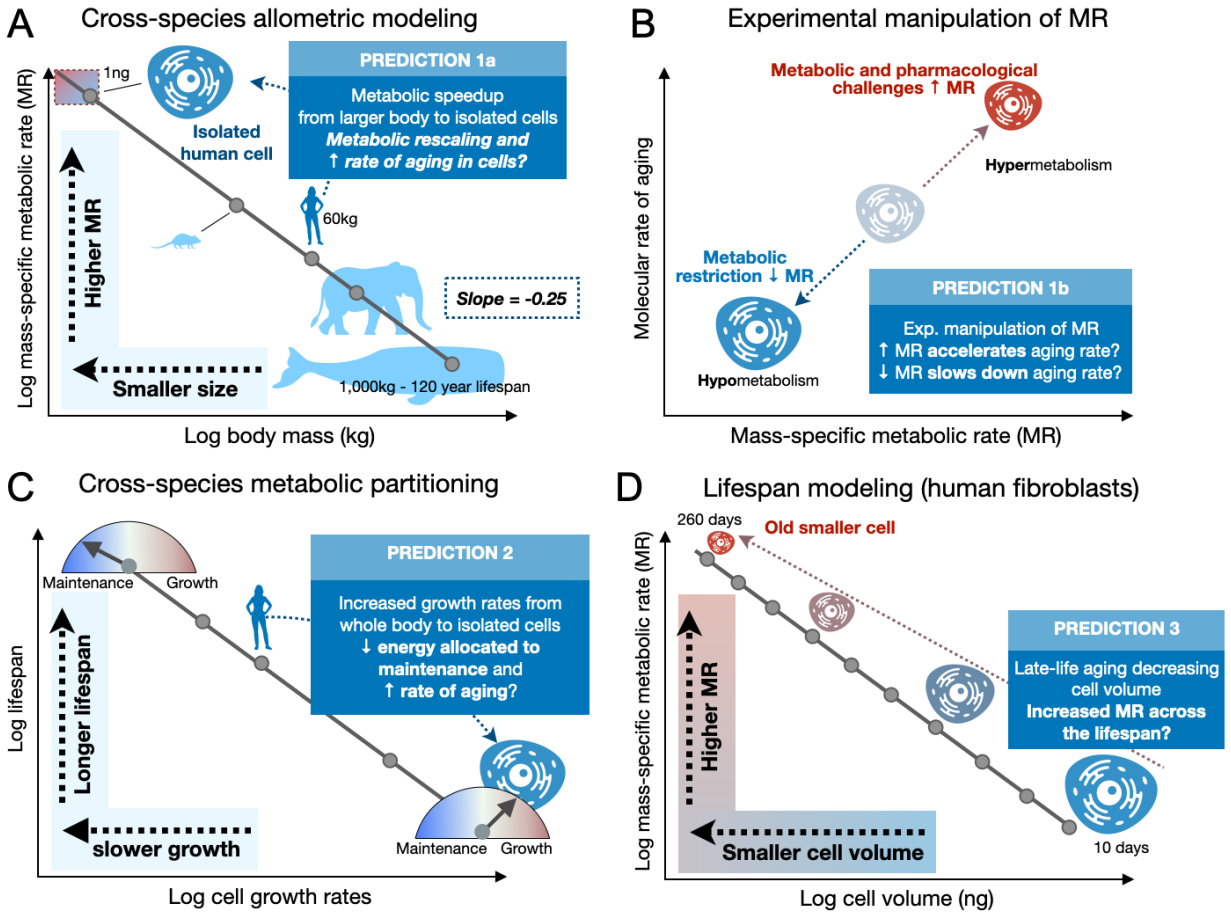

Figure 1. Allometric scaling laws and energetic partitioning away from maintenance predict accelerated aging in cultured human cells. (**A-D**) Theoretical schematic of four allometric rescaling hypotheses addressed in the current study. (**A**) Size scaling with mass-specific metabolic rate: As the size of an organism increases there is a 3/4 rescaling of MR. Here we ask whether this rescaling continues when cells are isolated from the body and placed in culture. (**B**) Experimental manipulation of MR (increase or decrease) should predictably alter the rate of cellular aging in primary human fibroblasts. (**C**) Metabolic partitioning of an organism's finite energy budget between growth and maintenance, and effects on lifespan. As the growth rate increases, the amount of energy devoted to maintenance and repair processes decrease and consequently the lifespan of the organism decreases. (**D**) Expanded scaling region denoted by dotted box in (A). Volume rescaling across the cellular lifespan: As cells get older their volume and MR should follow a further rescaling predicted by energetic demand equations.

Box 1 Theoretical Predictions of Metabolic Aging

I) Metabolic scaling, growth dynamics, and maintenance costs

Across mammals of different adult mass, M, metabolic rates, B, have been shown to follow $B \propto M^{3/4}$ (West, 2018). This empirical argument has been argued to be the consequence of the structure of optimal vascular networks which regulate the flow of resources to tissues (West et al., 1997, 1999). A variety of previous efforts have derived growth rate from metabolic rate by considering that the total energy budget of an organism is partitioned between growth and maintenance purposes:

$$B_0 V^{\alpha} = E_v \frac{dV}{dt} + B_v V \tag{1}$$

where E_v is the energy required to synthesize a unit of new biomass, and B_v is the metabolic rate required to maintain an existing unit of biomass. This equation can be solved for the growth trajectory of a single organism (e.g. West et al., 2002; Moses et al., 2008; Kempes et al., 2012), and it can also be used for finding the growth rate of an organism. This equation can be rewritten in terms of the growth dynamics as

$$\frac{dV}{dt} = \frac{B_0}{E_v} V^{\alpha} - \frac{B_v}{E_v} V. \tag{2}$$

Because $\alpha = 3/4$, this equation shows that the amount of energy devoted to maintenance, $B_v V$, will be an increasing in time and will eventually be the entire metabolism when an organism reaches maturity. This corresponds to the metabolic homeostasis observed during early the early phase of the tissue cultures and provides a baseline against which to compare late-life departures **(Figure 3)**. Equations 1 and 3 have also been used at the cellular level (Kempes et al., 2012) where one can write:

$$\frac{dV_c}{dt} = \frac{B_0}{E_v} V_c^{\alpha} - \frac{B_v}{E_v} V_c. \tag{3}$$

This form allows us to interpret the effective costs of cells, B_0, B_c, and E_v using our direct measurements of total metabolism, $B = B_0 V_c^{\alpha}$, and cell volume, V_c, along with calculations of growth rate, dV_c/dt, obtained from the time-series of V_c **(Figures 3, S2)**.

II) Lifespan and cellular rates

It has also been shown that lifespans follow $L \propto M^{1/4}$ (Speakman, 2005). To consider the metabolism of cultured cells we can use the fact that the number of cells is proportional to mass, $N_c \propto M$, such that the cellular metabolic rate is given by $B_c = B/N_c \propto M^{-1/4}$ (West et al., 2001, 2002). Taken together this implies that across mammals of different size every unit of mass receives the same total energy over a lifetime since $B_c \cdot L \propto M^0$ is a constant.

Prediction 1: This also shows that cellular lifespans, L_c, are inversely proportional to cell metabolic rates since $L \propto B_c^{-1}$ and $L_c \propto L$ and thus $L_c \propto B_c^{-1}$ **(Figures 5)**.

Additional work that has focused on the detailed accounting of damage and repair over the life course of an organism to understand aging (Hou, 2013). We can extend these ideas to the cellular level to consider the lifespan consequences of cellular energetic shifts where lifespan should follow

$$L = \frac{C}{B_c \left(\delta / V_c - \eta\right) + \eta E_v \frac{dV_c}{dt}} \tag{4}$$

where C is the critical fraction of damaged organism mass, δ indicates how much damage is associated with a unit of metabolic expenditure, and η gives the fraction of maintenance metabolism dedicated to repair.

Prediction 2: Ignoring the constants, Equation 4 shows that lifespan will decrease if either B_c or $\frac{dV_c}{dt}$ increase. If B_c remains roughly constant between adults and cell cultures, as we observe, and if cellular growth rates increase substantially, then $L \propto \left(\frac{dV_c}{dt}\right)^{-1}$, that is, lifespan will decrease proportionally to increasing growth rate **(Figures 2, 3)**.

III) Cell volume and metabolic rate

Interspecifically there are several possibilities for the connection between body mass, cell size, and cellular metabolic rate. These possibilities are bounded by a constant cell size with a cellular metabolic rate that follows $B_c \propto M^{-1/4}$ to a constant cellular metabolic rate with cell sizes that follow $V_c \propto M^{1/4}$ (Savage et al., 2007). From the perspective of aging it is important to consider what happens to cells after they have reached adult size and metabolic homeostasis. For example, it has been shown that humans lose mass later in life (Kuo et al., 2020; Pontzer et al., 2021). If we assume that all lose of mass comes from a decrease in cellular mass while preserving the number of cells, then we would have that $B_c \propto M^{-1/4} \propto V_c^{-1/4}$, where we consider that $m_c \propto V_c$. This result also predicts that the mass or volume specific metabolic rate of cells will follow $B_c/V_c \propto V_c^{-5/4}$ and equivalently $B_c \propto V_c^{-1/4}$.

Prediction 3: Once a consistent metabolic rate is reached in a population of cells, then any decrease in cell volume will be accompanied by an increase in metabolic rate following $V_c^{-1/4}$ as observed in our data **(Figures 3, S8)**.

Hidden References: (Moses et al. 2008; Savage et al. 2007; G. B. West, Brown, and Enquist 1997; Geoffrey B. West, Brown, and Enquist 1999; G. West 2018; G. B. West, Brown, and Enquist 2001; Pontzer et al. 2021; Kuo et al. 2020)

Cellular isolation increases resting metabolic rate

In humans, the basic metabolic cost of life measured as the resting metabolic rate (MR) is ~1,500 kcal/day, which is generated from oxygen consumption at a rate of 3.5-3.8 mlO_2/min/kg of body weight, equivalent to 0.057 watts/kg (Taivassalo et al. 2003; Jeppesen et al. 2009; Davies 1961). During maximal exercise (VO_{2max}), humans on average achieve a MR of 43 mL O_2/min/kg or 0.64 watts/kg (Kaminsky et al. 2021), representing a ~11-fold dynamic range at the whole-body level. The highest ever recorded VO_{2max} is 96 mL O_2/min/kg or 1.44 watts/kg (Haugen et al. 2018), corresponding to a dynamic range of >25-fold from rest. These resting and maximal human MRs provide a baseline from which to compare MR in substantially smaller, isolated cells of the same species.

We performed indirect MR measurements in primary cultured human dermal fibroblasts for up to 260 days of cellular lifespan from five healthy donors (3 female and 2 male, 0-36 years old, **Extended Data Figure 1A**). To derive stable estimates of MR after cellular isolation, we estimated total ATP synthesis rates from both oxidative phosphorylation (oxygen consumption rate, OCR) and glycolysis (extracellular acidification rate, ECAR) (Mookerjee et al. 2018). We initially restricted these analyses to the first 2-5 weeks in culture to avoid effects of replicative aging while maintaining a large sample size. The resting MR of primary human fibroblasts was 1.34 watts/kg, equivalent to the amount of energy used by the whole body at rest (**Figure 2A**). If we consider that cells with high MR (e.g., beating heart cardiomyocytes, brain neurons) and low MR (e.g., skin fibroblasts) unequally contribute to whole body MR, based on tissue-specific MRs (Wang et al. 2010; Davies 1961) a better estimate of resting fibroblast MR *in vivo* would be 0.85 watts/kg (**Supplemental File 1**). According to this estimate, the isolation of skin fibroblasts from *in vivo* to *in vitro* increased cell-specific MR by ~1.8-fold, although more sensitive estimates of *in vivo* fibroblast rates in dedicated studies are needed and could shift this factor. Regardless of the baseline estimate, these results demonstrate that our human fibroblasts at least maintained their resting MR. However, because the cells are non-confluent the division rates dramatically increase relative to *in vivo* (**Extended Data Figure 1C-E**).

To compare mass-specific *maximal* MR between cells and the whole body, we next measured maximal MR by uncoupling the inner mitochondrial membrane (FCCP) and blocking the mitochondrial ATP synthase (oligomycin). This combination maximizes the rate of oxygen

consumption and elevates glycolytic ATP production close to its maximal capacity. Analyzing maximal relative to resting MR showed that isolated fibroblasts operated at approximately half of their maximal energy production capacity (**Figure 2B**), compared to the 11-25-fold spare capacity of the organism *in vivo*. Together, the relatively high mass-specific resting MR and reduced dynamic energetic range of primary human fibroblasts suggest that isolated *in vitro* cells exhibit a markedly elevated resting energy expenditure (REE) relative to *in vivo* tissue.

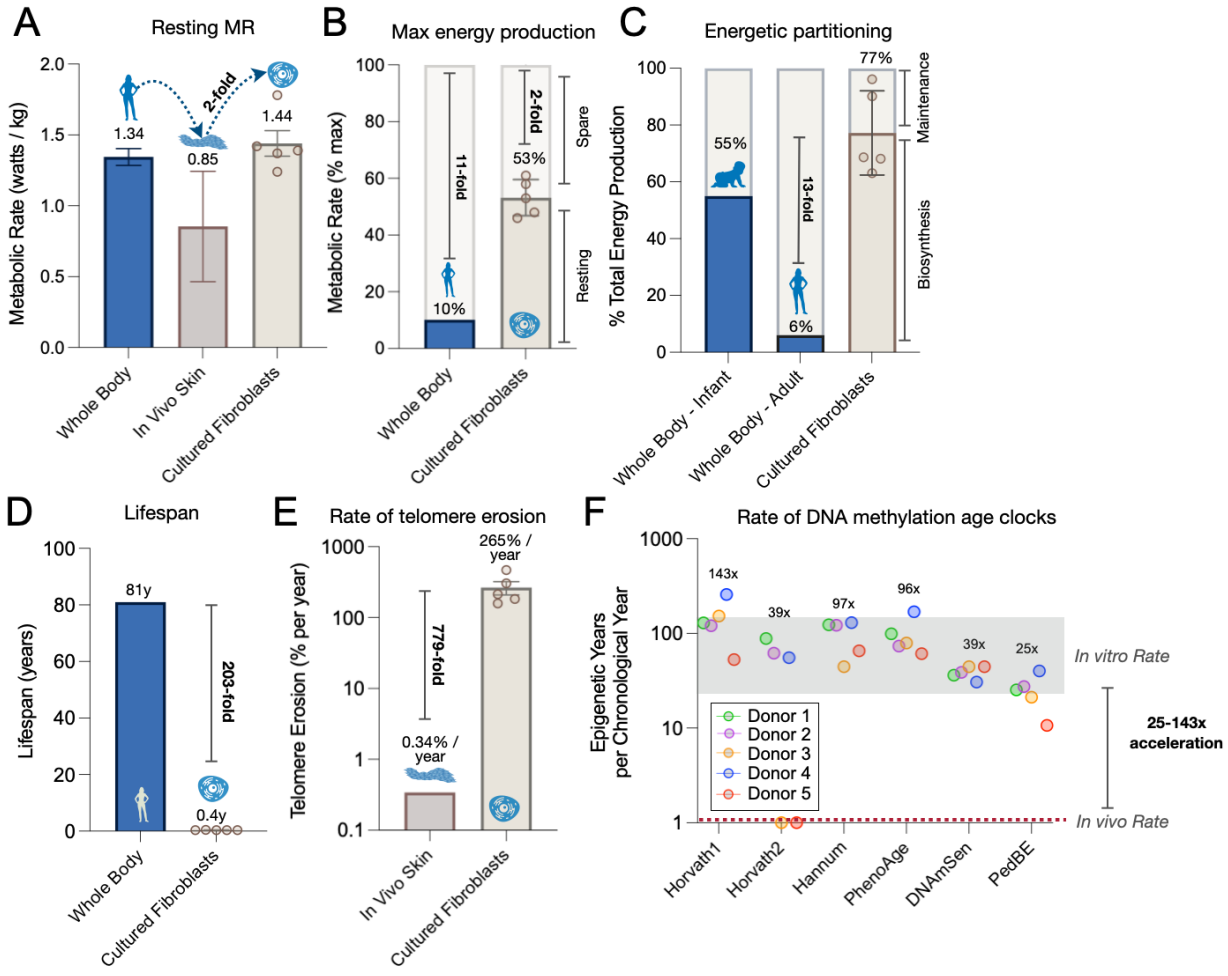

Figure 2. Comparison of *in vivo* and *in vitro* metabolic rates, and rates of biological aging. (**A**) Average MR for the human body, skin tissue (derived values), and primary cultured fibroblasts. Whole body and skin values derived from indirect calorimetry (n=2-3 studies ± S.E.M for independent sources per tissue, see *Methods* and *Supplemental File 1* for details). *In vitro* cellular MR was measured in five primary human fibroblast lines from healthy donors ages 0-36 years using extracellular flux analysis (Seahorse, n=5 donors ± S.E.M, using transformation into metabolic rates from (Mookerjee et al., 2018)). (**B**) Spare oxidative capacity of the whole body and cultured fibroblasts. Values are shown as the percentage of max MR determined by indirect calorimetry at maximal exercise intensity for whole body, and with the inner mitochondrial membrane proton ionophore FCCP for cultured fibroblasts. The reserve capacity of the system is highlighted as fold-change above resting values. (**C**) Energetic partitioning of maintenance and biosynthesis costs in whole body infants and adults, and cultured fibroblasts. Cellular rates are quantified during the linear growth phase (days 10-70, 4-5 timepoints per cell line) (**D**) Average lifespan of humans (defined as average mortality across industrialized

countries) and in cultured fibroblasts (defined as the time required to reach the Hayflick limit). Both definitions reflect the time over which the system (body or cell population) is self-sustainable. (**E**) *In vivo* telomere shortening rates in n=200 GTEx samples of 20-70 years old sun-exposed skin samples (Demanelis et al. 2020) compared to telomere shortening rates in cultured fibroblasts longitudinally quantified during the linear growth phase (days 10-70, 4-5 timepoints per Donor). (**F**) Rate of epigenetic aging in cultured fibroblasts (days 10-70, 4-5 timepoints per Donor) quantified with six validated epigenetic clocks trained to predict the rate of human aging *in vivo* (linear slope = 1 biological year per chronological year, red dotted line). Annotations indicate the average rate of biological aging across all donors for each clock, and the average *in vivo*-to-*in vitro* acceleration across all clocks. n=5 donors ± S.E.M for human fibroblasts.

Hypergrowth predicts accelerated aging and shortened lifespan of cultured cells

In vivo, lifespan is defined as the length of time an organism remains a self-sustaining unit, after which death occurs and the system breaks down (Jones et al. 2014). Similarly, for *in vitro* replicating fibroblasts, lifespan can be conceptualized as the Hayflick limit, quantified as the total number of cell divisions achieved before senescence occurs. In both contexts, the lifespan ends when the system loses its ability to be self-sustaining. Using the energetic partioning equations of Box1.I, we estimate that during cellular isolation from the body, fibroblasts shifts from ~6% to ~77% of total energetic budget towards biosynthesis processes during cellular (**Figure 2C**). Compared to a multi-kilogram body, the combined effects of increased metabolic rate and shifted biosynthesis partitioning, micron-scale cells in culture would be predicted to have substantially reduced lifespans. As expected for replicating fibroblasts, cells underwent near complete growth arrest (i.e., quiescence or senescence) after 148.0±4.9 days, representing approximately 0.4 years of life (**Figure 2D & Extended Data Figure 1B**). Compared to the average human lifespan (81 years) (Bank 2017), this *in vivo* to *in vitro* transition represents a ~203-fold reduction in lifespan. Deploying an epigenetic-based algorithm to count cell divisions (i.e., mitotic clock, (Youn and Wang 2018)) to fat and skin tissue samples from female donors ages 40-85 years (Grundberg et al. 2013), we calculated that on average in an adult human the time to divide is 537 days, while in our cell cultures the time to divide in the early phase of the cultures is 1.44 days (**Extended Data Figure 1C-E**). Given the limited shift in cellular metabolic rate demonstrated above, this energetic repartioning towards growth predicts a rescaling of lifespan by a factor of 322 which is comparable in scale to the observed factor of 203.

Consistent with well-established molecular features of replicative senescence (Campisi 1997), we observed marked telomere shortening over the first 100 days of growth. Compared to physiological aging of skin where telomeres erode at a rate of 0.00093% per day (i.e., 0.34% per year) (Demanelis et al. 2020), relative telomere length of cultured skin fibroblasts decreased by 0.73% per day (**Figure 2E & Extended Data 1H**). Relative to *in vivo* rates, this represents a

~779-fold acceleration of telomere erosion *in vitro*, a difference that is, in part, attributable to more frequent genome replication *in vitro*.

We also measured genome-wide DNA methylation (DNAm, EPIC platform) longitudinally at multiple timepoints during the lifespan of each cell line, which allows for the estimation of epigenetic age using algorithms or "clocks" trained to accurately predict age in the human body (Sturm et al. 2019). In human tissues, DNAm clocks predict 1 year of epigenetic age for each calendar year (i.e., slope of 1) with high accuracy (r>0.95) (Levine et al. 2018; Horvath 2013; Hannum et al. 2013; Horvath et al. 2018; McEwen et al. 2020; Levine et al. 2019). However, in cultured fibroblasts, DNAm clocks return slopes ranging from 25-143 biological years per chronological year (**Figure 2F**). We further calculated epigenetic aging rates for principal component (PC)-based clocks (Higgins-Chen et al. 2021) which revealed a more stable and consistent acceleration of 44-58 biological years per chronological year *in vitro* relative to *in vivo* (**Extended Data Figures 2A-C**). Together these clocks reveal that *in vivo* epigenetic aging markers are conserved in the replicative portion of the lifespan *in vitro*, and importantly the rate of epigenetic aging is accelerated by an average factor of ~50x in isolated cells. Put simply, a week of aging *in vitro* is approximately equivalent to a year of aging *in vivo*.

Aging-related volume reduction and increased mtDNA density

We next describe the cytometric dynamics across the replicative lifespan, lasting up to 260 days (**Figure 3A**). Across the lifespan, as cells entered quiescence and senescence, population doubling rate decreased progressively from 0.6-0.8 (first passage) to fewer than 0.01 (last passage) divisions per day. Early in life during the linear growth phase, long-lived cells maintained relatively constant cell volume. In the latter portion of the lifespan, although cells appeared larger (covering a larger surface area) when imaged in their adherent state, optimal measurements of floating cell diameter showed that the volume of aging fibroblasts declined by 57-83% towards the end of life (average=-72.5%, p<0.0015, **Figure 3B-C**). All cell lines reached a similar lower limit of cell size, suggesting an inherent minimum biological size limit of ~2000μm^3 in this cell type. We further estimated the molecular density of cells across the lifespan by combining total protein, RNA, and DNA per cell, which did not reveal any stable age-related trend in cell density. (**Extended Data Figure 3A**). According to the allometric relationship of mass and MR, this reduction in cell size would predict an increase in cell-specific MR. Accordingly, we observed an increase in the number of mtDNA copies per cell (mtDNAcn) across the lifespan (**Figure 3D**). As cells aged, they accumulated 113-347% more copies of mtDNA (average=+178.1%, p<0.0014, **Figure 3E & Extended Data Figure 3B**). Since cell

volume decreased with aging, the density of mitochondrial genome per unit of cellular volume increased by a striking 2.7-12.1-fold across the cellular lifespan (**Figure 3F**), foreshadowing substantial bioenergetic recalibration among aging cells.

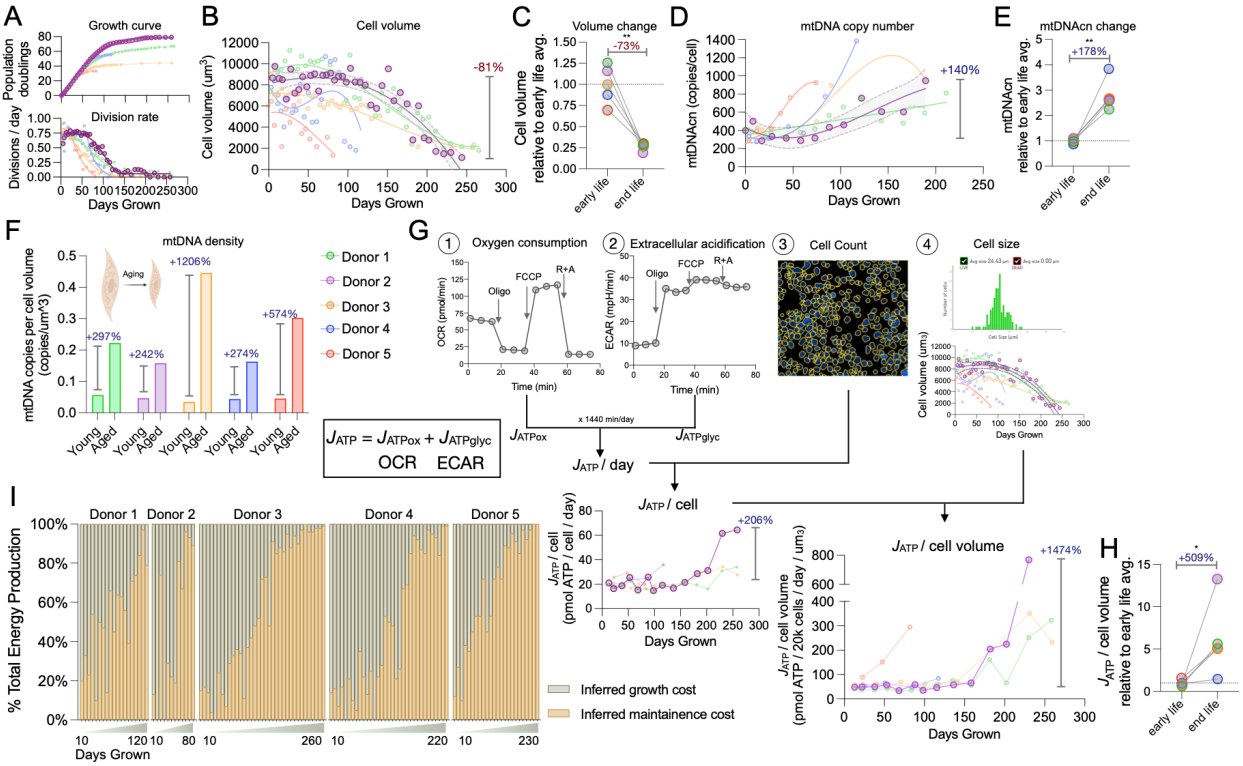

Figure 3. Lifespan trajectories of cellular bioenergetics and maintenance cost. (**A**) Cumulative population doubling (*top*) and doubling rates (*bottom*) measured across the replicative lifespan for all fibroblast lines (n=5 donors). The longest-lived cell line, Donor 2 (*purple*), is highlighted for clarity. (**B**) Absolute cell volume change (polynomial fit, 95% confidence interval) and (**C**) percent loss from early to late life (n = 7-23 timepoints per cell line). (**D**) Longitudinal trajectories for the absolute number of mitochondrial DNA copies per cell (mtDNAcn), (**E**) average percent change from early to late life, and (**F**) intracellular mtDNA density (normalized to cell volume) for young and aged fibroblasts. (**G**) Schematic of metabolic rate (MR) measurements derived from parameters measures using the Seahorse XF^{e}96. (G1-2) Raw oxygen consumption rate (OCR) and extracellular acidification rate (ECAR) are converted into OxPhos-derived (J_{ATPox}) and glycolysis-derived ($J_{ATPglyc}$) ATP production rates, respectively, and combined into total ATP production rate ($J_{ATPtotal}$). MR measures are then normalized to the number of cells in each measurement (E3), and the average cell volume at each passage (E4). Applied to longitudinal trajectories in each donor, this yields the total ATP consumption/production rate per cell volume ($J_{ATP\text{-}Total}$ /cell volume) and closest available estimate of mass-specific metabolic rates. (**H**) Average change in $J_{ATP\text{-}Total}$ /cell volume (total MR) from early life to end of life across the 5 donors. (**I**) Fractions of total energy production devoted to maintenance and growth costs modeled using energy budgeting equations (see Box 1.II). Note the reduction in growth-related costs as cell division rates approach zero at the end of the lifespan. All values are interpolated from a piecewise first-order model. Two-tailed paired ratio t-test, * $p < 0.05$, ** $p < 0.01$.

Aged fibroblasts show exponential rise in metabolic rate

By concurrently measuring MR and cell size, we derive energy expenditure per unit volume. The volume-specific MR was ~58.1 J_{ATP} / μm_3 in early life. All donors examined

exhibited volume-specific MR within a relatively narrow range (40.4-57.2, C.V. = 12%), with the exception of Donor 2's short-lived fibroblasts, which exhibited a high MR (**Figure 3G**). Remarkably, small inter-individual variations in initial MR per unit volume inversely correlates with the final Hayflick limit of a given cell line, where volume-specific MR explains 67% of the variance (r^2) in the maximal number of population doublings (**Extended Data Figure 4A**). This high correlation is on par with the many other metrics of replicative lifespan including initial telomere length of a given cell line (r^2 = 0.73, **Extended Data Figure 4B-D**). The basal MR in young cells likely reflects the combined standard energetic cost of DNA replication, protein synthesis, osmotic regulation, and other vital processes (Buttgereit and Brand 1995; Kempes, van Bodegom, et al. 2017). The reduction in cell size reveals that cellular energy demand per unit of cell volume increases by up to 15-fold from early to late life ($p<0.014$, avg. 509% increase, **Figure 3H**). This age-related rise in MR is disproportionately due to glycolysis-derived ATP ($J_{ATPglyc}$). Whereas young cells derive on average 39% of total J_{ATP} from glycolysis, $J_{ATPglyc}$ contributes on average 63% of total J_{ATP} in late life (**Extended Data Figure 3C**). Also consistent with this, mitochondria-derived J_{ATPox} relative to mtDNAcn revealed that in aged fibroblasts, the mitochondrial ATP output per mtDNA copy was on average 58% lower, pointing to lower "efficiency" of each mitochondrial genome (**Extended Data Figure 3D**). The age-related 5-fold increase in MR likely reflects cell-wide compensatory processes that could be explained either by the induction of new synthesis and growth activity (e.g. replication and division), or a global increase in the energetic costs of repair processes and maintenance due to molecular damage or other energy-dependent processes (e.g., protein secretion and signaling).

Using the growth model described in **Box 1.I** we then determine the total energy usage devoted to growth and maintenance costs (**Figure 3I & Extended Data Figure 3E**). Despite total energy production increasing exponentially at the end of lifespan, the maintenance cost begins to increase gradually across the lifespan, shifting from <10% of total energy consumption in young cells to >90% after growth arrest. Thus, growth costs decrease across the lifespan, with increasing maintenance costs accounting for the majority of the age-related rise in MR.

Age-related secretion factors contributing to maintenance *costs*

This age-related increase in maintenance cost could be explained by the expected rise in signaling proteins released from aged quiescent cells known as the senescence associated secretory profile (SASP) (Coppé et al. 2010). To characterize the secretory activity of aging cells across the lifespan, we designed a custom Luminex cytokine array designed based on

comprehensive proteomics characterization of aging human plasma (Tanaka et al. 2018). Of the 27 cytokines detected in extracellular media, we found that compared to young cells (<50 days grown), aged cells (>150 days grown) secreted on average ~11.4-fold higher amounts of cytokines on a per-cell basis, including several pro-inflammatory cytokines, chemokines, and proteoglycans which require translation and post-translational modifications (Payea et al. 2021) (**Figure 4A-B**). Upregulated cytokines included the canonical pro-inflammatory cytokines IL-6 and IL-8. The age-related metabokine GDF15 was also secreted in a time-dependent manner, exponentially rising 15-fold ($p<0.011$) across the cellular lifespan, consistent with changes occurring in aging human plasma (**Figure 4C**). We further measured the release of cell-free mitochondrial DNA (cf-mtDNA) across the lifespan and observed an exponential rise (+10.6-fold, $p<0.0041$, **Figure 4D**). Parallel measurements of cell-free nuclear DNA (cf-nDNA) showed that the released mitochondrial-to-nuclear genome ratio was on average 8.3-fold higher in aged cells than young cells ($p<0.012$), indicating partially selective mtDNA release.

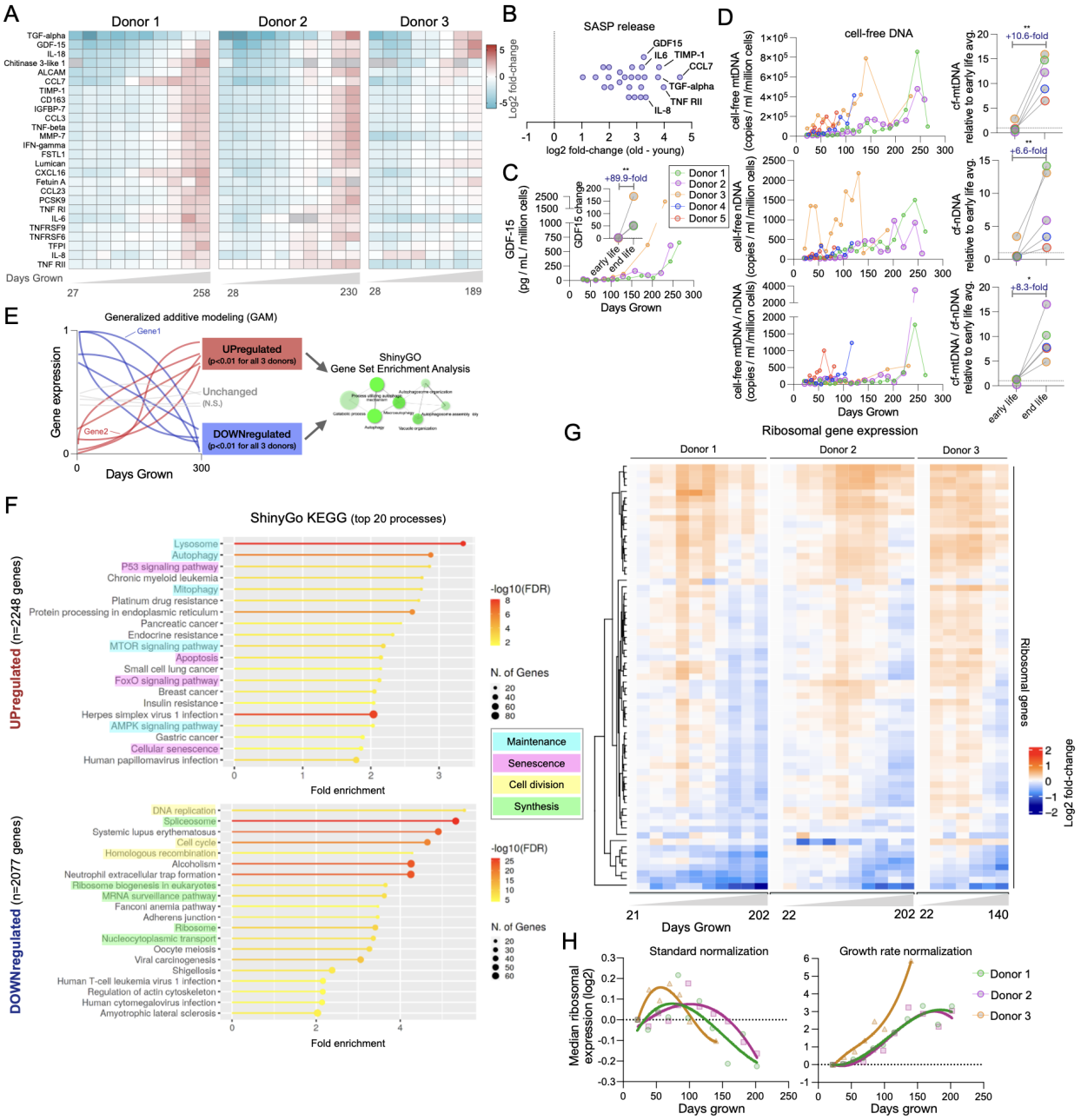

Figure 4. Age-related upregulation in maintenance and synthesis pathways. (**A**) Extracellular cytokine concentrations released on a per-cell basis, measured on two multiplex arrays across the cellular lifespan of Donors 1-3. Values are Log_2 median-centered for each cytokine; samples with undetectable values are shown as grey cells. (**B**) Median log_2 fold changes in extracellular levels of each cytokine from young to old fibroblasts, showing up to >20-fold upregulation for all cytokines. (**C**) Extracellular GDF15 across the cellular lifespan for Donors 1-3, with (*inset*) fold change relative to the early life average. (**D**) Cell-free mtDNA (*top*), nDNA (*middle*) and mtDNA/nDNA ratio (*bottom*) across the cellular lifespan. (*Right*) Summary plots show fold change relative to early life average for Donors 1-5. Two-tailed paired ratio t-test, * $p < 0.05$, ** $p < 0.01$. (**E**) Analytic strategy to identify overrepresented biological processes from RNAseq data where age-related genes (significant nonlinear change across the lifespan, generalized additive modeling, n=3 Donors, 7-11 timepoints/cell line) are grouped by the direction of change and analyzed in ShinyGo (v0.75). (**F**) Top 20 KEGG processes for both upregulated and downregulated genes. Color indicates fold enrichment, dot size indicates the number of genes

enriched in each process. Highlighted processes are categorized by shared biological function. (**G**) Lifespan trajectories of ribosomal subunit gene expression (RNAseq) centered to the median of the youngest control timepoints. (**H**) Median expression of all ribosomal subunits using standard normalized expression (*left*, data fitted with third order polynomials) and adjusted for population doubling rate (i.e., growth rate in cell divisions per day, *right*), highlighting the disproportionate expression of biosynthesis machinery relative to growth rates.

Gene expression changes for synthesis and maintenance pathways

To gain further insight into the potential origin of increased maintenance costs beyond increased secretory activity, and to examine transcriptional changes associated with increased MR, we sequenced bulk RNA across the lifespan in 3 of the 5 cell lines (~8 timepoints per cell line, **Figure 4E**). We then performed gene set enrichment (GSE) analysis on the age-related genes identified by generalized additive modeling (nonlinear trajectories) using both KEGG (**Figure 4F & Supplemental Files 4-5**) and gene ontology (GO) processes (**Extended Data Figure 5 & Supplemental Files 6-7**). Age-related upregulated genes belonged to several canonical maintenance pathways: 'Lysosome' (fdr=7.8e-9, KEGG:04142), 'Autophagy' (fdr=7.8e-7, KEGG:04140), 'Mitophagy' (fdr=3.6e-3, KEGG:04137), and 'mTOR signaling pathway' (fdr=2.2e-3, KEGG:04150) (Figure 4F). Similarly, enriched gene ontology (GO) processes amongst upregulated genes included 'Autophagy' (fdr=8.0e-9, GO:0006914), 'Vacuole organization' (fdr=3.8e-6, GO:0007033), and 'Protein transport' (fdr: 5.8e-6, GO:0015031), consistent with the hypersecretory phenotype (Extended Data Figure 4). Downregulated genes mainly mapped to protein synthesis pathways: 'Ribosome biogenesis in eukaryotes' (fdr=2.6e-15, KEGG:03008) and 'Ribosome' (fdr=2.6e-15, KEGG:03010) (Figure 4F). Enriched GO processes amongst downregulated genes included: 'Cellular biosynthetic process' (fdr=2.6e-15, GO:0044249), 'Gene expression' (fdr=3.6e-19, GO:0010467), and 'Translation' (fdr=2.9e-15, GO:0006412) (**Extended Data Figure 5**). This hypothesis-free enrichment analysis supports our model's predictions for age-related increase of maintenance costs and simultaneous decrease in growth costs.

The age-related changes of ribosomal content were further examined using the transcript levels of all ribosomal subunits (**Figure 4G**). Interestingly, ribosomal mRNA expression shows a biphasic trajectory, increasing during the stable growth phase (when cells divide at a constant rate) until the inflection point when division rate slows down, then declining rapidly upon the induction of senescence (see **Supplemental File 8** for additional cellular processes). However, in actively dividing cells, a substantial portion of the ribosomal machinery is produced to supply both daughter cells (i.e., growth-related), whereas in non-dividing cells all

the ribosomal machinery can be actively devoted to (maintenance-related) protein synthesis. Therefore, to estimate the proportion of ribosomal machinery available for maintenance-related protein synthesis, we normalized transcript levels per growth rate (i.e., population doubling rate). This correction highlights a continuous, cell division-independent rise in ribosomal gene expression (**Figure 4H**). One interpretation of this result is that it reflects the preparatory buildup of translation machinery in aging cells, commensurate with the rising maintenance costs.

We further defined the age-related gene expression changes for mtDNA-encoded genes (**Extended Data Figure 6A**). By categorizing all 37 genes into their RNA species type (mRNA, rRNA, or tRNA), we show a preferential increase in mitochondrial tRNA and rRNA genes, while mRNA are stably expressed with age (**Extended Data Figure 6B**). Because the number of mtDNA copies per cell increased by 518%, this reflects a 53% decrease of mRNA yield per mtDNA molecule (**Extended Data Figure 6C**), which could be explained by either a decrease in mtDNA transcription or loss of mRNA stability in aging cells.

Transcriptomics and methylome rescaling from in vivo to in vitro systems

Next we quantified the degree of global speedup (i.e., rescaling) that occurs when moving cells from the human body (*in vivo*) to cell culture (*in vitro*). *In vivo* transcriptomic and methylome data was aggregated from publicly available cross-sectional studies of skin, the tissue of origin for our fibroblast. The datasets used include GTex postmortem skin biopsies (RNAseq, n=520, ages 20-70) and TwinsUK Biobank skin punch biopsies (DNAm arrays, n=322, ages 40-85). *In vitro* gene expression and DNAm data were both collected from our cultured fibroblasts across the cellular lifespan (n=3 donors, 7-14 timepoints per cell line, 3-265 days grown). Since we are primarily interested in the overall rates of change in gene expression or DNAm levels in noisy data, we fit the data using a linear regression to impose the least number of assumptions. In these regressions, slopes establish the rates of global change per unit of time, both *in vivo* and *in vitro*. Genes and methylation sites were filtered to include those that significantly change with age (fdr<0.05), and slopes obtained across the entire lifespan to reflect the rate of change with chronological age. Rescaling factors reflecting the difference between isolated cells vs the human body were then estimated as the ratio of the median slope of age-related *in vivo* and *in vitro* markers (**Extended Data Figure 7A**).

To account for the high-variability of cross-sectional *in vivo* data, we quantified rescaling factors using increasingly more stringent models (**Extended Data Figure 7B**), which included linear regression, min/max confidence intervals (min-max CI), linear mixed effects (LMER), and permutation modeling (see methods for further details). Rescaling factors ranged from

~100-300x and DNA methylation data showed an average ~63x higher rescaling factors than gene expression data. Thus, regardless of the underlying model and modality (gene expression or DNAm), our analysis reveals a robust speedup of global molecular processes for cells growing in culture.

We further assessed how the rescaling factor changes depending on which portion of the cellular lifespan was used for rate estimations (**Extended Data Figures 7C-D**). Due to the longitudinal design of our *in vitro* datasets, generalized additive modeling (GAM) was performed to identify nonlinear age-related genes and DNAm markers. This restriction ensured that the same genes and CpG sites were used to quantify rescaling factors and did not have any bias toward a particular portion of lifespan. The *in vivo*-to-*in vitro* speedup indexed by rescaling factors peaked in early to mid-phase of cellular lifespan. Across both RNAseq and DNAm datasets and regardless of how age-related markers were selected, the late-phase of cellular lifespan, when division rate is lowest, showed the lowest rescaling factor, with a reduction in rescaling factors by 46 and 72% relative to early life, respectively. This result indicated that as cells approach growth arrest, they exhibit a global slowdown of gene expression and methylation dynamics. To validate this observation, we used an entirely orthogonal computational approach and estimated the rate of unspliced to spliced mRNA by RNAvelocity (Manno et al. 2018) for each sample across cellular lifespan (**Extended Data Figure 8**). Global splicing-related factors was previously shown to be downregulated with cellular aging and regulates the onset of replicative senescence (Kwon et al. 2021). RNAvelocity confirmed that the greatest period of speedup occurred in early life and subsequently decreased by an average of 60% during replicative arrest. This result suggests that accelerated replication may contribute to approximately half of the *in vitro* speedup of biological aging. Nevertheless, these results demonstrate that even at the end of life, when there is a near absence of cell division, fibroblasts still exhibit a speedup of molecular processes of at least ~100x relative to age-related rates observed in the human body.

MR experimental manipulations speed up and slowdown of rate of cellular aging

The framework in Box 1 predicts that in addition to increasing growth rates an increase in cellular metabolic rates will also decrease lifespan. Thus, we assessed if we could alter the degree of *in vitro* rescaling and rate of aging by directly modulating metabolic rate while keeping growth rates in a similar range (**Extended Data Figure 9A-B)**. We used a set of established genetic, pharmacological, and environmental treatments that put the cells in either a hypermetabolic (increased MR) or hypometabolic (decreased MR) state (**Figure 5A**) (Sturm,

Monzel, et al. 2021). Hypermetabolic treatments included chronic 1nM oligomycin (Oligo, +134% MR), chronic 100nM dexamethasone (DEX, +150% MR), chronic mitochondrial nutrient uptake inhibitors (mitoNUITs, +110% MR), and fibroblasts taken from SURF1-mutant patients (+106% MR). Hypometabolic treatments included chronic 2-deoxy-d-glucose treatment (2DG, -27% MR) and contact inhibition (-10% MR) (**Figure 5B**). All treatments reduced growth rates by 10-88% which represents a shift shifted by less than a factor of two in comparison to the 373 fold increase from *in vivo* (**Extended Data Figure 9A**) but growth rates were not significantly correlated with MR (p=0.40, r^2 = 0.04, **Extended Data Figure 9B**), suggesting that division rates and energy expenditure are not inextricably coupled. These results reinforce the notion of Box 1 Equation 4 that the molecular speedup *in vitro* can be caused by either increased cellular metabolic rates or increased division rates.

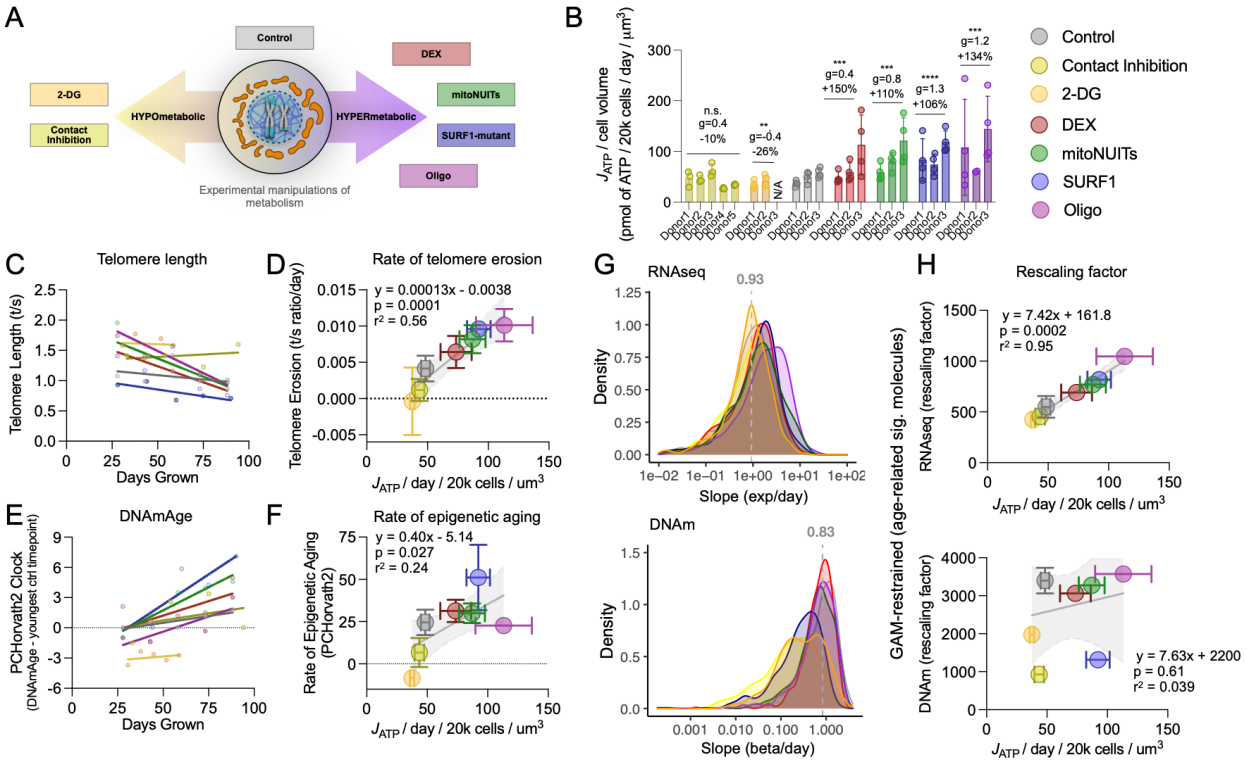

Figure 5. Experimental manipulation of metabolic rate rescales *in vitro* biological aging rates. (**A**) MR-modulating treatments and (**B**) effects on volume-specific metabolic rates between 25-95 days grown (linear phase of growth). Each bar represents a donor, and each data point is a different timepoint. N/A indicates missing data for 2DG-treated Donor3. *Contact Inhibition* = induction of growth arrest and quiescence through contact inhibiting; *2-DG*, chronic 1mM 2-deoxy-d-glucose; *DEX*, chronic 100nM dexamethasone; *mitoNUITs,* chronic combination of mitochondrial nutrient uptake inhibitors; *SURF1-mutant,* fibroblasts from pediatric patients *SURF1* mutations; Oligo, chronic 1nM oligomycin (see *Methods* for details). (**C**) Illustrative relative telomere length trajectory (25-95 days grown, for Donor 2 and SURF1_1) used to derive the rate of telomere shortening across MR-altering treatments. (**D**) Correlation between MR and the rate of telomere erosion across all donors (error bars are S.E.M. across donors; linear regression with 95% confidence intervals). (**E**) Baseline-adjusted trajectory of DNAmAge (PCHorvath2, also known as Skin&Blood clock) for the

same samples as in (C), and (**F**) correlation between MR and epigenetic aging. (**G**) Frequency distribution of the slopes for the rate of change for all expressed genes (*top*) and methylated CpG sites (*bottom*) for a given MR-altering treatment. Gray line: median slope of untreated cells. (**H**) Correlation of MR with rescaling factors (*in vivo*-to-*in vitro* acceleration of molecular processes) across all age-related genes (*top*) and CpG sites (*bottom*, linear regressions with 95% confidence intervals), highlighting the strong association between volume-specific MR and age-related gene expression changes.

We then tracked how these MR modulators affected cellular aging and rescaling measures. Volume-specific MR was linearly correlated with the rate of telomere erosion ($p<0.001$, $r^2=0.56$) and with the rate of epigenetic aging (PCHorvath2, $p<0.05$, $r^2=0.24$) (**Figure 5C-F**). Additionally, experimentally-induced elevation in MR were linearly correlated with gene expression derived rescaling factor ($p<0.001$, $r^2=0.95$) but not DNAm ($p=0.61$, $r^2=0.04$) (**Figure 5H**), meaning that treatments that increased MR also increased the rate at which age-related gene expression changes occur. Note the hypometabolic treatments were able to slow down the rate of methylation changes but hypermetabolic treatments failed to further increase the rate of change beyond untreated cells. This may be because the DNAm changes occurring in controls are already proceeding at or near their maximum rate of change, such that no additional metabolic speedup can further accelerate these rates.

We further measured the proportion of speed-up induced by cell division by partially recapitulating the multicellular environment of tissues (increasing cell-cell contacts and reducing cell division rates) through contact inhibition (**Extended Data Figure 9C**). Contact inhibition reduced both RNAseq and DNAm rescaling factors by -58% and -85%, respectively. This suggests that over half of speedup from cell culturing was caused by physical isolation and continuous replication, and the remaining 42% and 15% for RNAseq and DNAm, respectively, was dependent upon other unidentified physiological factors.

Finally, we directly assessed the conservation of the size scaling inverse power law originally found cross-species, to metabolically-altered human fibroblasts (**Extended Data Figure 9D**). We find that despite large shifts in cell volume, up to 73% loss between treatments, the metabolic size scaling coefficient of -0.25 originally found cross-species was maintained across time and treatment groups *in vitro* (**Extended Figure 9E**). Similarly, despite the large shifts in division rate and Hayflick limit, we observed a remarkable temporal alignment between the inflection points at which growth arrest occurs and volume-specific MR rises at the end of life, regardless of the intervention used (**Extended Data Figure 10**). This finding highlights the robust temporal interconnection of hypermetabolism (i.e., excess metabolic rate relative to an organism's optimum) and cellular senescence, which is consistent with the connection between metabolic and growth rates (Kempes, Dutkiewicz, and Follows 2012). We therefore extend

allometric size scaling predictions to cell culture, where smaller cells exhibit predictable increases in MR and commensurate alterations in lifespan trajectories.

DISCUSSION

We have generated a longitudinal, high-temporal-resolution dataset of bioenergetic, cytological, and genome-wide molecular dynamics in primary fibroblasts from multiple human donors to quantify the rate of biological aging in parallel with MR. This experimental system established three main predictions based off the allometric theory of metabolism: 1) when isolated from the body, human cells exhibit an increased rate of cellular division, allocate a substantially smaller fraction of their energy budget to maintenance, and correspondingly age faster based on multiple molecular markers; 2) over the course of the cellular lifespan, primary human fibroblasts acquire a striking hypermetabolic phenotype in late stages (>100-fold increase in volume-specific MR) characterized by increased maintenance costs, and associated with increased mtDNA genome density, upregulation of extracellular secretion, and maintenance-related transcriptional programs (e.g., autophagy); and 3) manipulating MR with mitochondria-targeted metabolic, genetic, and pharmacological perturbations predictably alters the molecular rate of aging, providing experimental evidence for the interplay of MR and aging in a human system. We hypothesize that these rescaling principles emerge in cultured cells when they are compared to cells in the human body that are able to age at a significantly slower rate owing to the collective partitioning of biological functions across multiple functionally specialized cell types and organs, making the overall state of living more energetically efficient (Nespolo, Mejias, and Bozinovic 2022; Jang et al. 2019). These findings have important implications for a number of unresolved questions in geroscience and medicine, which we discuss below.

Energetic perspective of cellular aging

This work compliments the replicative theory of cellular aging and emphasizes an alternative perspective based on energetics. This energetic perspective predicts the life course of cultured cells on par with measures of telomere length. Our experimental data indicates that MR-altering perturbations regulate the rate of telomere shortening and biological aging based on molecular (gene expression and DNA methylation) dynamics, and thus suggests that MR and its partioning may play a causal role in aging and lifespan regulation. Moreover, the late phase of the lifespan was marked by substantial hypermetabolism, which could also contribute to the onset of quiescence and senescence programs. This contribution could be in addition to, or in parallel with other factors, such as telomere length generally believed to dictate replicative potential. Our experiments rule out the contribution of varying oxygen levels, as previously reported in OxPhos-deficient fibroblasts (Sturm, Karan, et al. 2021). Therefore, one would

expect that preventing the age-related increase in MR-associated mitochondrial components could mitigate aging phenotypes, a prediction in line with the fact that mitochondria are required for the acquisition of senescent phenotypes (Correia-Melo, Marques, and Anderson 2016).

Although this system by no means captures the full physiological complexity of aging, we nonetheless show wide scale shared age-related changes in molecular processes between *in vivo* and *in vitro* aging. These include epigenetic clocks trained in a variety of tissues, telomere shortening, global gene expression signatures, and DNA methylation at single genomic locations. The high degree of similarity among age-related trajectories in gene expression and DNAm *in vitro* and *in vivo* was the basis for our rescaling factors. All of these processes show that upon isolation and culturing, human cells exhibit a unanimous speedup of aging events at a rate 50-300x faster than when they existed in the human body. This is consistent with expectations from theory since lifespans are expected to be inversely proportional to either mass-specific metabolic rate (cellular metabolic rate) or cellular division rate under a fixed cellular metabolic rate (Hou 2013). Our work here illustrates that shifts in either cellular metabolic rates or how energy is partitioned will both affect lifespan. Specificaly, we see aging rates of cells increase when we increase the growth rates of cells under a fixed energy budget or increase cellular metabolic rates directly.

These speedups are in line with evidence from physiological aging where similar connections to metabolic rate have been described. For example, in humans, elevated resting MR (basal metabolic rate, BMR) is a risk factor for mortality (Ruggiero et al. 2008; Jumpertz et al. 2011; Schrack et al. 2014); correspondingly, lower BMR is associated with healthier and longer lifespans (Schrack et al. 2014). Mitochondrial diseases that trigger energetically costly integrated stress responses both *in vivo* and *in vitro* among fibroblasts similarly cause a speedup of molecular and physiological processes (e.g., elevated heart rate), have elevated MR, and dramatically reduced lifespan (Sturm, Karan, et al. 2021). This relationship has been further documented in cells exposed to chronic glucocorticoid signaling (Bobba-Alves et al. 2022) and obesity (Tencerova et al. 2019). Similarly, interventions such as exercise and calorie restriction, have been shown to lower MR through a process known as metabolic compensation (Careau et al. 2021), which may account for their health and lifespan benefits in humans (Pontzer 2018). Likewise, *C. elegans* have been shown to follow a temporal scaling of lifespan across environmental and genetic interventions including diet, temperature, and stress. Interestingly, this temporal scaling arises independently of any specific molecular target, thus suggesting a whole-organism control system such as metabolic rate enabling predictable stretching or shrinking of lifespan trajectories across perturbations (Stroustrup et al. 2016).

Overall, the speedup of isolated human fibroblasts mimics the cross-species relationships of size, cellular replication rates, MR, and lifespan. Our findings are further in line with the relationship between size and metabolism of fibroblasts from different sized dogs (Jimenez et al. 2018; Brookes and Jimenez 2021). Moreover, amongst invertebrates, smaller organisms with higher metabolic rates have been documented to have slowed time perception (perceive more units of time each second) (Healy et al. 2013). This observation further links metabolic rate to the biology of time perception - both *in vivo* and *in vitro*, where our data suggests that the fundamental ability of cultured fibroblasts to generate time- or age-related molecular recalibrations (i.e., to perceive time) may be based in their metabolic rates.

Potential mechanism of speedup

The question remains as to why higher metabolic rates and cell isolation leads to shorter lifespans? Our data supports both i) cumulative damage and ii) evolutionary programmed aging.

The damage mechanism of aging postulates that as cells grow they accumulate damage proportional to the total amount of metabolic activity (G. West 2018; Hou 2013). Correspondingly, an increasing percentage of a cell's energy budget is used for repair and turnover of cellular machinery with age. This hypothesis has been justified from the scaling relationship that total metabolic expenditure over a lifespan is constant across organisms of vastly different sizes and can even be used to predict invariant cancer risk across organisms (G. B. West, Brown, and Enquist 2001; Geoffrey B. West, Woodruff, and Brown 2002; Kempes, Dutkiewicz, and Follows 2012; Kempes, West, and Pepper 2020). This perspective proposes that as metabolic rate shifts, so do all of the other cellular rates, including growth and damage, such that a single cell always experiences the same lifetime totals but reached at different rates. Here we provide a much more direct validation of the theory by showing that over the cellular lifespan there is an age-dependent metabolic switch from growth to maintenance processes.

For evolutionary considerations of aging, which need not be in conflict with the damage hypothesis, there is a long history of proposed mechanisms including: i) the inability of natural selection to operate on late-life traits, ii) programmed death as a way to benefit populations, or iii) fundamental tradeoffs between life-history traits that benefit young individuals but later detract from older individuals (Mitteldorf 2010; Ljubuncic and Reznick 2009; Gavrilov and Gavrilova 2002). In the context of our work here it is important to note that all of these mechanisms will be affected by a rescaling of the physiological clock. If there are problematic late-life traits that have not been selected against by evolution these will simply be reached more quickly, and the same would be true for programmed death. Similarly, since most

life-history traits scale with metabolic rate across organisms of different sizes, it is reasonable to assume that metabolic rate would adjust the rates associated with life-history tradeoffs that produce aging. All three proposals are consistent with our finding showing a striking temporal alignment of rising metabolic costs and rapid reduction in cell division (see **Extended Data Figure 10**).

Regardless of the underlying reason for cellular aging and considering that many of these mechanisms could be fundamentally interconnected and co-optimized by evolution, we speculate that cells in the human body are able to age at a significantly slower rate because of the collective partitioning of biological functions across multiple functionally specialized tissues and organs, making the overall state of living more energetically efficient. For example, in populations of syngeneic yeast, metabolite exchange where some cells produce and consume different metabolites creates a state of metabolic cooperation that extends lifespan of individual cells within the population (Correia-Melo et al. 2022). In cells and animal communities, cell growth and fitness follow a density-dependent relationship known as the Alee effect (Kramer, Berec, and Drake 2018). Imposing severe isolation by culturing human cells at very low density impedes growth and compromises survival, even of cancer cells (K. E. Johnson et al. 2019). Long-lived mammalian organisms also exhibit extensive metabolic cooperation, where specific organs are responsible for the transformation and synthesis of specific metabolites and hormones, which are supplied at no or little cost to the cells and tissues consuming them (Jang et al. 2019). Thus, various cell types operate as an integrated network of metabolically and physiologically interconnected units, from which emerges a greater state of metabolic efficiency and lower resting metabolic rate per unit of body mass (Geoffrey B. West, Woodruff, and Brown 2002). In contrast, the spatial isolation and relative uniformity of cell monocultures would represent a more metabolically stressful state, where each cell must subserve every function necessary for its own survival. Further evidence for this explanation comes from hibernating organisms, where across five orders of magnitude in mass, the cellular metabolic rate of hibernation is lower than the lower limit of MR in isolated mammalian cells (Nespolo, Mejias, and Bozinovic 2022). This notion also draws from evidence in regenerative biology where cohabiting cells within the organism behave as an interconnected collective driven by computations taking place at the whole-body level, rather than at the single-cell level (Levin 2021). This understanding implies that experimentally adding energetic constraints that mimic the *in vivo* environment, such as contact inhibition and nutrient turnover, can lower energetic pressure and allow cells to live longer.

As discussed, a few different factors could contribute to the age-related hypermetabolism. Here we identify maintenance-related processes as the main driver, specifically mitochondrial content accumulation with decreased energy-production efficiency, and upregulation of autophagy and extracellular secretions. These drivers of hypermetabolism include transcriptional activation of several stress response pathways and the production and secretion of cytokines and chemokines, notably the metabokine GDF15, which is the most robustly upregulated circulating protein in the blood of aging humans (Tanaka et al. 2020). We find that the secretion of an average cytokine is roughly 1% of metabolic rate, implying that as few as 100 high-abundance secreted cytokines (Basisty et al. 2020; Tanaka et al. 2018) could dominate the cellular energy budget. Here we also report a novel senescence-associated secretory molecule, cell-free mtDNA, a signature that matches cross-sectional lifespan findings in human blood (Pinti et al. 2014). Other processes that could not be measured in this study, including molecular repair and degradation processes, ion cycling across membranes, and cell migration could also contribute to the exponential rise in energetic costs at the end of life - even in the absence of cell division.

Previous work has established an upper limit of Gibbs free energy (Yang et al. 2021; Niebel, Leupold, and Heinemann 2019), where flux redistribution allows the cell to switch between different energy pathways (i.e., respiration and fermentation) but is ultimately limited and must avoid a critical Gibbs energy dissipation rate. Our data suggest that although cells within the organism operate at only 5-10% of maximal rates, cultured cells operate much closer to this upper limit (~50%). If this upper limit is imposed by physical constraints on metabolism, the fidelity of molecular operations, and on cell division (Morowitz 1978; DeLong et al. 2010; Lan et al. 2012; Kempes, Dutkiewicz, and Follows 2012; Kempes, Wolpert, et al. 2017; Yang et al. 2021), this could explain: i) the 258-fold reduction in lifespan of cultured cells, ii) why cells slow down rates of change as they enter quiescence (see **Extended Data Figure 7D**), and iii) why treatments that induced higher MR failed to speedup DNAm rescaling factors any further (see Figure 5H). In support of this, and congruent with our results indicating increased production and secretion of protein material in old cells, human fibroblasts in replicative senescence were brought out of senescence by mildly inhibiting protein synthesis (Takauji et al. 2016), thus freeing up a portion of the energetic budget. Thus, our results are internally consistent with a link between total energy flux or MR, and lifespan regulation.

However, recent work in rodents suggests that temperature, rather than MR, may be a more important determinant of lifespan (Zhao et al. 2022). Elevating body temperature reduces lifespan, even in the context of reduced MR. In cultured fibroblasts, although the overall

temperature of the cellular system should be well-controlled at 37°C, we cannot rule out the possibility that intracellular temperature could be affected in parallel with MR. This may be particularly relevant since mitochondria are the warmest compartment of the cell, operating at temperatures estimated around 50°C (Chrétien et al. 2018). Thus, a complete mechanistic model of the MR-lifespan connection, which is beyond the scope of the current analysis, will likely need to incorporate both MR and temperature. In addition, it has also recently been shown in *C. elegans* that other factors such as stressors, as well as temperature, adjust the rate of aging (Stroustrup et al. 2016). Amazingly, organisms appear to follow a universal aging curve rescaled by these various environmental, energetic, and stress factors (Stroustrup et al. 2016), and this work should be integrated with our perspective here to understand how multiple effects adjust aging in humans beyond the basic energetic arguments.

Age-related cell size and shape changes

Here we find that aging fibroblasts get smaller in size as they age. On the surface this finding contradicts the aging of human stem cells (Mitsui and Schneider 1976) where replicative age is associated with larger size. However, Lengefeld et al. (Lengefeld et al. 2021) found that aged stem cells show similar decreased growth and increased maintenance pathways with replicative aging. These differences in age-related size changes may instead reflect different strategies among different cell types, whereby stem cells rely on glycolytic-derived metabolism attempt to maintain dormancy and proliferative potential by diluting cellular contents (Neurohr et al. 2019), as opposed to fibroblasts (boht *in vitro* and *in vivo*) which rely heavily on high-growth OxPhos-derived metabolism to increase cell density in support of the epithelial structure. We also note that rather than recede towards the most thermodynamically neutral and efficient shape, the spheroid, aged primary human fibroblasts adopt a characteristic flattened morphology with substantially greater complexity and covering greater surface area than young cells (see **Extended Data Figures 11**). Greater shape complexity entails increased surface area, which incur energetic cost associated with maintaining ionic balance across the plasma membrane, as well as energetic costs associated with producing and maintaining physical membrane deformations. This morphological response could also be indicative of energetically challenged cells trying to uptake more resources, again owing ultimately to increased maintenance costs. Thus, a number of unaccounted processes could be contributing to age-related hypermetabolism.

Lifetime MR trajectories

Our longitudinal age-related trajectories demonstrating profound bioenergetic recalibrations across the cellular lifespan agree with recent work in a single cell line of WI-38 human lung fibroblasts, indicating the increased abundance of OxPhos, TCA, and carbon metabolism proteins and transcripts across cellular passages, in parallel with the upregulation of glycolysis in senescence (Chan et al. 2022). The age-related increase in MR across the lifespan also is in line with a recent report demonstrating, in mice, an age-related elevation in both resting MR and MR associated with a given workload (i.e., metabolic efficiency) (Petr et al. 2021). In other words, in this system as in our fibroblast model, metabolic efficiency declines and the total energetic cost of living increases with age. The increased cost of living is also in keeping with human physiology, including the increased mRNA splicing activity that increases in skeletal muscle with aging (Ubaida-Mohien et al. 2019; Ferrucci et al. 2022; Tumasian et al. 2021).

However, this finding is in contrast with resting and free-living whole-body MR in aging individuals where lifetime measures of body mass and MR appear to decrease in later life (Ruggiero et al. 2008; Schrack et al. 2014; Pontzer et al. 2021; Kitazoe et al. 2019). We speculate that the contrast between our cellular system and the *in vivo* situation may reflect shared bioenergetic constraints at both the cellular and organismal levels, but which are met via different strategies. In cultured cells, the adaptive strategy appears to consist of reducing (and eventually halting) the rate of cell division, thus freeing MR and a portion of the ATP budget for maintenance processes, as well as reducing cell volume, which should similarly decrease total metabolic demand. Accordingly, cells with higher MR have markedly lower Hayflick limits and slow division rates. In the aging human body, similar bioenergetic constraints and cellular recalibrations likely occur and may cause, in addition to the atrophy of some energy-consuming tissues (e.g., brain, muscles) in old age, integrated multi-system responses involving endocrine, metabolic, neural, and behavioral recalibrations that contribute to improving efficiency and decreasing MR among the organ network. This would include, for example, reduced physical activity levels and intensity. It should also be noted that while the mass-specific metabolic rate is maintained across adulthood, older adults lose a significant amount of weight (Pontzer et al. 2021; Kuo et al. 2020; Yeakel, Kempes, and Redner 2018). Differences between *in vivo* and *in vitro* MR trajectories across the lifespan could also be explained by survivor bias. Old frail individuals may in fact show decreased body mass and an exponential rise in MR (as seen in culture) but die soon after or are not in sufficiently good health condition to be included in the aforementioned population studies of healthy individuals. These accelerated timescales of

cultured lifespan may therefore reflect the late-life frailty period in human years which remains out of reach of epidemiological studies.

Following the predictions made from cross-species scaling laws established at the organismal level (**Box 1.III**), this work extends allometric theory to the cellular level and establishes the interconnected speedup of energetic and molecular processes in cultured human cells. The current study provides an alternative perspective of cellular aging inspired by allometric and metabolic theory, which opens up many new possibilities for the role of energetics in cellular aging.

Limitations

Looking forward, there are a few important factors that should be considered to provide a complete picture of metabolic rescaling that occurs upon cell isolation. First, to fully integrate our results with the cross-species perspectives it is important to recognize that humans are metabolic outliers in the allometric scaling of body size and lifespan, exhibiting roughly 4x longer lifespans than most species of similar size (Pontzer et al. 2021). Correcting for this deviation and understanding its origin could be useful for future intercomparisons with mice or other model organisms. Second, comparing MR and aging rates between cultured fibroblasts and whole body dermal skin measurements is imperfect, limited by the heterogenous mixture of cell types typical of skin tissue (e.g., fibroblasts, macrophages, adipocytes, mast cells, Schwann cells, and stem cells), although fibroblasts are the principal cell type of the dermal layer (T. M. Brown and Krishnamurthy 2021). We further note that our *in vitro* measurements are taken from cell populations including millions of cells, such that our data reflect population-level measurement and not single cells. Our results are therefore comparing a group of cells with some of the properties of a complete tissue. This may explain why many of the aging signatures in our fibroblasts mirror whole-body cross-species expectations. The *in vivo* MR estimates of skin from indirect calorimetry are also imprecise, as it is not possible to precisely isolate skin from other organs. This likely leads to imprecision in the *in vivo* to *in vitro* comparison of MR. Third, we note that there is no known way to directly manipulate MR without off-target effects to other biological processes. MR reflects the integrated state of the system rather than a single, modifiable process. Thus, the MR-altering conditions included in **Figure 5** have unavoidable confounding effects on multiple cellular features that should be considered in the interpretation. Nevertheless, the convergence of results across a spectrum of genetic, metabolic, and pharmacological perturbations increase our confidence in the robustness and generalizability of our findings. Finally, while it is reasonable to assume that energy budgets are fundamentally

limiting to organisms, and thus metabolic rate should proportionally adjust all molecular clocks, the explicit mechanisms between metabolic rate and cellular aging will need to be revealed by future work.

Methods

All *in vitro* data presented in this paper is part of the 'Cellular Lifespan Study' which is described in detail in Sturm et al., 2021 (Sturm, Monzel, et al. 2021), including a more thorough description of all methods. A portion of these data examining the hypermetabolic and accelerated aging effects of primary OxPhos defects (SURF1 mutations and Oligo treatment) are reported in (Sturm, Karan, et al. 2021), and the effects of chronic dexamethasone treatments are reported in (Bobba-Alves et al. 2022).

In vitro fibroblast cultures

Human fibroblasts were obtained from local-clinic (IRB #AAAB0483) and commercial distributors from five healthy donors (**Table 1**) and stored in liquid nitrogen before culturing. Cells were cultured in T175 flasks (Eppendorf #0030712129) at standard 5% CO_2 and atmospheric O_2 at 37°C in DMEM (5.5 mM physiological glucose) supplemented with 10% FBS (Thermofisher #10437010), 50 µg/ml uridine (Sigma-Aldrich #U6381), 1% MEM non-essential amino acids (Life Technologies #11140050), 10 µM palmitate (Sigma-Aldrich #P9767) conjugated to 1.7 µM BSA (Sigma-Aldrich #A8806), and 0.001% DMSO (treatment-matched, Sigma-Aldrich #D4540). For metabolic rate measurements in Seahorse analyzer (Agilent), cells were grown in complete XF media without pH buffers and supplemented with 5.5 mM glucose, 1 mM pyruvate, 1 mM glutamine, 50 µg/ml uridine, and 10 µM palmitate conjugated to 1.7 µM BSA to ensure that cells have access to a variety of energetic substrates.

Cell line name	Received from	Source tissue	Sex	Donor age	Passage	Cat#
Donor1 (HC1, hFB12)	Lifeline Cell Technology	Dermal breast	male	18	1	FC-0024 Lot # 03099
Donor2 (HC2, hFB13)	Lifeline Cell Technology	Dermal breast	female	18	1	FC-0024 Lot # 00967
Donor3 (HC3, hFB14)	Coriell Institute	Foreskin	male	0	4	AG01439
Donor4 (HC5, hFB1)	Hirano Lab	Dermal upper-arm	male	29	3	NA
Donor5 (HC6, hFB2)	Hirano Lab	Dermal upper-arm	female	26	4	NA

Cell line name	Received from	Source tissue	Sex	Donor age	Passage	Cat#
Patient1 (SURF1-1)	Hirano Lab	Dermal upper-arm	male	1	7	NA
Patient2 (SURF1-2)	Hirano Lab	Dermal upper-arm	male	11	5	NA
Patient3 (SURF1-3)	Hirano Lab	Dermal upper-arm	female	9	9	NA

Table 1. Cell line characteristics for all donors.

Cells were grown for up to 260 days by repeated passaging every 5-7 days. To determine the number of cells to plate at each passage, growth rates from the previous passage were used, pre-calculating the expected number cells needed to reach ~90% confluency (~3 million cells) by the next passage, ensuring relatively similar confluence at the time of harvesting for molecular analyses. Cells were never plated above 2.5 million cells to avoid plating artifacts of contact inhibition. Individual cell lines from each donor were grown until they exhibited less than one population doubling over a 30-day period, at which point the cell line was terminated, reflecting the end of the lifespan. The Hayflick limit was calculated as the total number of population doublings reached by the end of each experiment.

Repeat cellular lifespan experiments were performed three times (Study Phases II,IV,V) for Donors 1-3 under untreated conditions. In study phase V, cells were seeded to reach a lower maximum confluency of <80%.

Cytology

Cell counts, volume and proportion of cell death were determined in duplicates (CV <10%) and averaged at each passage using Countess II Automated Cell Counter (Thermofisher #A27977). Cell density measures were estimated by taking the weighted sum of total extracted protein (BCA assay, Bioworld #20831001-1), RNA (RNeasy kit, Qiagen #74104), and DNA (DNeasy kit, Qiagen #69506) at each timepoint. Further, at each passage, brightfield images were taken at 10x and 20x using an inverted phase-contrast microscope (Fisher Scientific #11350119).

Treatments

MR-altering treatments design, dose, and duration are listed in **Table 2**. In addition, contact inhibition was induced by allowing dividing cells to fill the culture flask (i.e., confluency), which reduces the growth rate by an average of 87% (from 0.65 to 0.085 div / day). This

induced a quiescent cell cycle arrest allowing the determination of time-dependent changes independent of cell division. Treatments began after 15-days of culturing post-thaw to allow for adjustment to the *in vitro* environment. Media was changed weekly and cells were placed in biohood the same amount of time for cells undergoing standard passaging.

Experimental treatments	Design	Concentration	Duration (days grown)	Solvent	Cat#
Dexamethasone (DEX)	Chronic addition to media	100nM	20-270	EtOH	Sigma-Aldrich #D4902
Oligomycin	Chronic addition to media	1nM	20-270	DMSO	Sigma-Aldrich #75351
mitoNUITs (UK5099, Etomoxir, BPTES)	Chronic addition to media	2μM, 4μm, 3μM	20-270	DMSO, ddH_2O, DMSO	Sigma-Aldrich #PZ0160, Sigma-Aldrich #E1905, Sigma-Aldrich #SML0601
2-deoxy-d-glucose (2DG)	Chronic addition to media	1mM	20-170	ddH_2O	Sigma-Aldrich #D3179
Contact inhibition	Cells achieve maximum confluence without passaging	NA	20-140	NA	NA
SURF1-mutant	Separate donors with inborn mutations	NA	0-150	NA	NA

Table 2. Experimental design of MR-altering treatments.
*Chronic indicates treatment was reapplied at each passage

Metabolic rates

Bioenergetic parameters of cultured fibroblasts were measured using the XFe96 Seahorse extracellular flux analyzer (Agilent) (Tan et al. 2015). Oxygen consumption rates (OCR) and extracellular acidification rates (ECAR, i.e., pH change) were measured over a confluent 20,000k cell monolayer every ~15 days, following the manufacturer's instructions. Respiratory states such as basal and maximum respiration rates were all determined using the MitoStress Test (Brand and Nicholls 2011) which involves the sequential additions of the ATP synthase inhibitor oligomycin (final concentration: 1 μM), the protonophore uncoupler FCCP (4 μM), and the electron transport chain Complex I and III inhibitors rotenone and antimycin A (1 μM). The final injection included Hoechst nuclear fluorescent stain (Thermofisher #62249) to allow for automatic cell counting using the Cytation1 Cell Imager (BioTek). Raw bioenergetic measurements were normalized to relative cell counts on a per-well basis.

ATP production rates from oxidative phosphorylation (OxPhos, J_{ATPox}) and glycolysis

($J_{ATPglyc}$), as well as total cellular ATP production and consumption ($J_{ATPtotal}$), were estimated using the method described by Mookerjee et al. (Mookerjee et al. 2018). Briefly, the method relies on the phosphate-to-oxygen (P/O) ratios of OxPhos and glycolysis, using oxygen consumption and proton production rates (PPR) as input variables. The same constants were used for all estimations, assuming glucose as the predominant carbon source and constant coupling efficiency. Changes in substrate consumption along the lifespan would require parallel assessments of metabolic flux to resolve. This assumption should have only a minor influence on calculated ATP production rates. We further note that maximum J_{ATP} measures were determined by adding the J_{ATPox} after FCCP injection with the $J_{ATPglyc}$ after oligomycin injection. We note that a separate metabolic assay would be required to assess true maximum glycolytic ATP production *in vitro*, which is beyond the scope of current experimental capacity. This metric of maximum energetic capacity is therefore limited and should be interpreted with caution (Schmidt, Fisher-Wellman, and Neufer 2021; Mookerjee et al. 2018).

Baseline whole body metabolic rates were obtained from indirect calorimetry in three small human cohorts reporting values consistent with literature norms (Taivassalo et al. 2003; Jeppesen et al. 2009; Rising et al. 2003). Max whole body MR (i.e., VO_2peak) estimates were obtained from Kaminsky et al. (Kaminsky et al. 2021). An estimation of skin-specific MR was calculated using Q_{O2} values for human *in vivo* tissues (see Table 4 in (Davies 1961). Additionally, skin-specific MR was calculated using the mechanistic model: REE = Σ(K(i) × T(i)), where REE is whole body resting energy expenditure measured by indirect calorimetry and T(i) is the mass of individual organs and tissues measured by magnetic resonance imaging (Wang et al. 2010). In this estimate, skin-specific MR is determined based on Elia's Ki values in which skin tissue Ki is estimated along with intestines, bones, and lungs, which together have Ki (12) similar to inactive skeletal muscle (13). To compare mass-specific MR *in vivo* to volume-specific MR in cultured fibroblasts, *in vivo* and *in vitro* units were converted using the attached **Supplemental File 1** ('SF1_Cell-to-Body_Oxygen_Consumption_Calculator'). This conversion assumes an average cell mass of 10ng (Geoffrey B. West, Woodruff, and Brown 2002; Park et al. 2008).

Estimation of growth and maintenance costs

Energetic budgets of growth and maintenance were estimated using the mathematical growth modeling originally describing unicellular organisms (Kempes, Dutkiewicz, and Follows 2012) which incorporates the basic energetic partitioning of the Pirt model (Pirt 1965) along with

metabolic scaling principles (Geoffrey B. West, Woodruff, and Brown 2002). See Equation 3 of Box 1 for calculation of the energetic budget of cultured cells.

Telomere length

Relative telomere length was evaluated on the same genomic material used for other DNA-based measurements. Measurements were performed by qPCR and expressed as the ratio of telomere to single-copy gene abundance (T/S ratio), as previously described (Cawthon 2002; Lin et al. 2010). Triplicate values of T and S for each sample were averaged to calculate the T/S ratios after a Dixon's Q test for outlier removal. The T/S ratio for each sample was measured twice.

Telomere length rates of erosion were calculated as the rate of change in T/S ratio per day grown from days 10-70 (Extended Data Figure S1H). Telomere erosion rates for physiological aging were obtained from the GTEx dataset outlined in Demanelis et al. (Demanelis et al. 2020), which contains relative telomere lengths of skin (sun-exposed) from donors ages 20-70 years old.

DNA methylation

DNA methylation markers were measured across the genome using the Illumina EPIC microarray (Illumina, San Diego). Briefly, DNA was extracted using the DNeasy kit (Qiagen #69506) and quantified using the QUBIT broad range kit (Thermofisher #Q32852). Extracted DNA was processed at the UCLA Neuroscience Genomic Core (UNGC) for bisulfite conversion and hybridization using the Infinium Methylation EPIC BeadChip kit. Data was processed in R (v4.0.2), using the 'minfi' package (v1.36.0), and normalized using functional normalization (FunNorm). RCP and ComBat adjustments using the 'sva' package (v3.12.0) were performed to correct for probe-type and plate bias, respectively. After quality control, DNAm levels were converted to beta values for 865,817 CpG sites.

Age-related DNAm changes were estimated using generalized additive modeling on individual DNAm sites using the R package 'mgcv' (v1.8-31). All genes that had a p-value < 0.001 across all three cell lines were identified as significant. Genes were separated into UPregulated and DOWNregulated lists based on the direction of age-related change. The full list of significant DNAm sites can be found in **Supplemental File 3.**

DNA methylation clocks and related measures

Epigenetic-based clocks were calculated using DNA methylation data (Horvath and Raj 2018) (**Table 3**). We computed three clocks designed to predict the chronological age, Horvath1 (i.e. PanTissue clock) (Horvath 2013), Horvath2 (i.e. Skin&Blood clock) (Horvath et al. 2018), Hannum (Hannum et al. 2013), and PedBE (McEwen et al. 2020) clocks; two clocks designed to predict mortality, the PhenoAge (Levine et al. 2018) and GrimAge (Lu, Quach, et al. 2019) clocks; a clock to measure telomere length, DNAmTL (Lu, Seeboth, et al. 2019); a clock designed to measure mitotic age, MiAge (Youn and Wang 2018); a clock trained to predict cellular senescence, DNAmSen (Levine et al. 2019), and two DNA methylation measure of the rate of deterioration in physiological integrity, DunedinPoAm (Belsky et al. 2020), and DunedinPACE (Belsky et al. 2022). The PC-based method replaces the clock's individual illumina probe measurements (5-500 CpGs) with the shared extracted variances among genome-wide CpGs from principal components (PC), yielding the PC-adjusted DNAmAges for each clock (Higgins-Chen et al. 2021).

Clock	Trained Usage	Source	Code
Horvath1 (PanTissue)	biological age	(Horvath 2013)	https://dnamage.genetics.ucla.edu/new
Horvath2 (Skin&Blood)	biological age	(Horvath et al. 2018)	https://dnamage.genetics.ucla.edu/new
Hannum	biological age	(Hannum et al. 2013)	https://dnamage.genetics.ucla.edu/new
PedBE	biological age (pediatric)	(McEwen et al. 2020)	https://github.com/kobor-lab/Public-Scripts/blob/master/PedBE.Md
PhenoAge	mortality	(Levine et al. 2018)	https://dnamage.genetics.ucla.edu/new
GrimAge	mortality	(Lu, Quach, et al. 2019)	https://dnamage.genetics.ucla.edu/new
DNAmTL	telomere length	(Lu, Seeboth, et al. 2019)	https://dnamage.genetics.ucla.edu/new
DNAmSen	replicative age	(Levine et al. 2019)	https://github.com/MorganLevineLab
PC-based (Horvath1, Horvath2, Hannum, PhenoAge, GrimAge, DNAmTL)	biological age, mortality, telomere length	(Higgins-Chen et al. 2021)	https://github.com/MorganLevineLab/PC-Clocks
MiAge	replicative age	(Youn and Wang 2018)	http://www.columbia.edu/~sw2206/softwares.htm
DunedinPoAM	rate of aging	(Belsky et al. 2020)	https://github.com/danbelsky/DunedinPoAm38

Clock	Trained Usage	Source	Code
DunedinPACE	rate of aging	(Belsky et al. 2022)	https://github.com/danbelsky/DunedinPACE

Table 3. Epigenetic clocks used to estimate the rate of biological aging based on DNA methylation dynamics.

In vivo DNA methylation data

TwinsUK DNA methylation data was obtained through the online GEO portal (GSE90124) collected as part of the TwinsUK study (Moayyeri et al. 2013). This dataset includes 322 skin samples collected by punch tissue biopsy of healthy female individuals ages 39-83 years old. Bisulfite-converted DNA from the 322 samples were hybridized to the Illumina HumanMethylation450 BeadChip. All 450,531 CpG sites of the 450k chip were present on the EPIC chip used for *in vitro* DNA methylation.

In vivo growth rates were obtained using the Mitotic Age clock (Youn and Wang 2018) on DNA methylation measured across the genome of adult skin and adipose tissue. The adipose dataset is made available by the TwinsUK Adult Twin Registry (ArrayExpress E-MTAB-1866) (Grundberg et al. 2013) and provides Illumina 450K DNA methylation data of 648 adipose obtained from females european-twins ages 40-85.

mtDNA copy number

mtDNA copy number was measured using a duplex qPCR as previously described (Picard et al. 2014). Briefly, duplex qPCR reactions with Taqman chemistry were used to simultaneously quantify mitochondrial (mtDNA, ND1) and nuclear (nDNA, B2M) amplicons. The final mtDNAcn was derived using the ΔCt method, calculated by subtracting the average mtDNA Ct from the average nDNA Ct. mtDNAcn was calculated as $2^{\Delta Ct}$ x 2, yielding the estimated number of mtDNA copies per cell. Note that mtDNA copy number was quantified on the same genomic material used for DNA methylation measurements.

Cell-free DNA

Cell-free mitochondrial (cf-mtDNA) and nuclear DNA (cf-nDNA) levels were measured simultaneously by qPCR on sampled media collected across cellular lifespan. Taqman-based duplex qPCR reactions targeted mitochondrial-encoded ND1 and nuclear-encoded B2M sequences as described previously (Ware et al. 2020; Belmonte et al. 2016; Trumpff et al. 2019). Each gene assay contained two primers and a fluorescent probe and were assembled as

a 20X working solution according to the manufacturer's recommendations (Integrated DNA Technologies). Digital PCR (dPCR) of the standard curve used in cf-mtDNA/cf-nDNA assessment were measured separately using singleplex ND1 and B2M assays using a QuantStudio 3D Digital PCR System and associated reagents (Thermo Fisher, cat#A29154) according to the manufacturer's protocol.

Cytokines

Two multiplex fluorescence-based arrays were custom-designed with selected cytokines and chemokines based on human age-related plasma proteins correlated with chronological age (Tanaka et al. 2018), and based on their availability on R&D custom Luminex arrays (R&D, Luminex Human Discovery Assay (33-Plex) LXSAHM-33 and LXSAHM-15, http://biotechne.com/l/rl/YyZYM7n3). Briefly, media samples were collected at each passage and stored at -80°C. Thawed samples were centrifuged at 500xg for 5 min and supernatant collected. Media samples were run undiluted on a Luminex 200 instrument (Luminex, USA) as per the manufacturer's instructions. Data was fitted and final values interpolated from a standard curve in xPONENT v4.2. Of the 51 measured cytokines, 27 were detected in the media of cultured cells. Cytokine concentrations were then normalized to the number of cells counted at the time of collection to produce estimates of cytokine production on a per-cell basis.

Gene expression

Gene expression was estimated by RNAseq selected for functional mRNAs using a Ribo-Zero Gold extraction protocol. Briefly, total genomic RNA was isolated every ~11 days across the cellular lifespan for control lines and selected treatments. RNA was stabilized using TRIzol (Invitrogen #15596026), stored at -80°C until extraction using a RNeasy kit (Qiagen #74104), quantified using the QUBIT high sensitivity kit (Thermofisher #Q32852), and underwent quality control on Bioanalyzer (Agilent RNA nano kit 6000, #5067-1511) and Nanodrop 2000. cDNA library preparation was performed using a Ribo-Zero Gold purification (QIAseq FastSelect -rRNA HMR Kit #334387) and NEBNext® Ultra™ II RNA Library Prep Kit (Illumina #E7770L). cDNA was sequenced using paired-end 150bp chemistry on a HiSeq 4000 instrument (Illumina, single index, 10 samples/lane, Genewiz Inc). Sequencing depth was on average 40 million reads per sample. Sequenced reads were then aligned using the pseudoalignment tool *kallisto* v0.44.0 (Bray et al. 2016), processed using txi import ('tximport', v1.18.0, length-scaled TPM), and vst normalized ('DEseq2', v1.30.1). Growth rate normalizations were performed using the median-centered doubling rates (divisions / day) at

each timepoint.

Gene Set Enrichment analysis (GSEA) was performed using the ShinyGO webtool (http://bioinformatics.sdstate.edu/go/, v0.75). Age-related changes were estimated using generalized additive modeling using the R package 'mgcv' (v1.8-31). All genes that had a p-value < 0.1 across all three cell lines were included in the analysis. Genes were separated into UPregulated and DOWNregulated lists based on the direction of age-related change. The full list of significant genes can be found in **Supplemental File 2.** Selected pathway gene sets (**Supplemental File 8**) were obtained from https://maayanlab.cloud/Harmonizome/. Expression values were centered to the median of youngest control timepoints and then transformed to a log2 scale. For ribosome-related analyses, ribosomal genes were selected from the KEGG database at https://www.genome.jp/kegg/pathway/hsa/hsa03010.html.

Rates of gene splicing and degradation can be derived from the relative abundance of unspliced (nascent) and spliced (mature) mRNA quantified by RNA-sequencing. These relative abundances can then be transformed into RNAvelocity, a high-dimensional vector that predicts the future state of cell identity on a timescale of hours (Manno et al. 2018). RNAvelocity has been used to track cellular lineage transitions, circadian rhythms, neurogenesis, embryogenesis development, and tissue regeneration using single-cell sequencing of tissue populations containing multiple cell types (Bergen et al. 2020; Manno et al. 2018). The computational pipeline for obtaining RNAvelocity estimates was as follows: RNAseq fastq files were aligned using STAR v2.7 (https://github.com/alexdobin/STAR/) to a pre-curated annotation of the hg19 genome (Lareau and Brenner 2015) to obtain spliced and unspliced RNA reads. RNAvelocity estimates of mapped reads were then quantified using the velocyto.py smart-seq command (https://velocyto.org/velocyto.py/) which treats each bulk RNAseq sample as if it were a single-cell from a SMART-seq experiment. All further analysis of velocyto output was performed in a Jupyter notebook adapted from the scVelo pipeline (https://scvelo.readthedocs.io/VelocityBasics.html).

In vivo gene expression data

In vivo RNAseq data was obtained from the Genotype-Tissue Expression (GTEx) study (Lonsdale et al. 2013) through the online dbGaP accession #phs000424.v8.p2, under the project #27813 (Defining conserved age-related gene expression trajectories). This dataset includes 12,767 samples obtained postmortem from organ donors across 54 unique tissues from n=980 individuals (653 men, 327 women), ages 20-70 years. Data was filtered to the tissue

'Skin - Sun Exposed (lower leg)', yielding 520 samples (330 men, 178 women) ages 21-70 years.

Rescaling factors

Rescaling factors were obtained using the rates of change in global gene expression and DNA methylation markers in *In vivo* and *In vitro* data (see schematic in Extended Data Figure S5A). *In vivo* data was obtained from the GTEx and TwinsUK studies. Age-related markers were identified through linear modeling across lifespan in both datasets with a cutoff of 0.1 p-value. Genes and DNAm markers were then grouped by direction of change with age (increase or decrease with age) and then the overlap of markers between the *in vivo* and *in vitro* datasets moving in the same direction with age were selected for final calculations. The rescaling factor was calculated as the ratio of the median *in vitro slopes* to the median of the *in vivo* slopes.

We note several assumptions that need to be considered when evaluating our MR-altering rescaling factor results (**Figure 5G**): i) we use independent genes and methylation sites for each treatment group that are significantly changing with age. An alternative approach of preselecting nonlinear GAM molecules and then estimating slopes off that list was attempted and showed similar results. ii) the final rescaling factor was further documented as the median of all overlapping significant molecules and excludes the rates of change in genes or sites that do not change with age. iii) we report the slopes of only genes and molecules that share the same directional change between *in vitro* and *in vivo* datasets. An alternative approach of measuring our rescaling factors on the union of both *in vitro* and *in vivo* age-related genes and sites was performed and showed minimal difference to our final findings. iv) our analysis assumes that dermal fibroblasts are comparable to biopsies of skin samples, which contain a heterogeneous mixture of fibroblasts, epidermis, and epithelial cells. v) For *in vitro* treatments, the derived slopes for each molecule were taken from the same time period of 25-95 days grown. This portion was selected to ensure a) at least 3 timepoints were included for each donor, b) that the treatment had fully taken effect (treatment started at 15 days) and c) that there were matching timepoints with close to equal distributions of samples in each treatment group. We also note that the treatment 2DG was only performed on 2 donors (Donors 3 & 4) and the SURF1-mutant cells involved comparing entirely different donors with an inherited genetic mutation(s) that could have had developmental effects.

Rescaling factor modeling for In vivo data

In vivo rates of change were estimated using four parallel approaches: i) linear regression, ii) linear mixed effects, iii) min-max confidence intervals, and iv) permutation modeling. Linear regression was performed using R (v) built in lm function. Linear mixed effects modeling was performed using the 'lmer' function from the R package 'lme4' (v1.1) with a fixed effect for age and random effects for type of collection (postmortem or organ donor), donor relationship (i.e. twin, sibling, etc.), and sex of donor. Significance values were determined using an ANOVA to a null model with the same random effects. Min-max confidence interval slope estimation was determined by taking the minimum and maximum of the 95% intervals at the first and last timepoint of a linear regression of the *in vivo* data. The slope was then estimated as the maximum absolute linear slope from either the minimum of the first timepoint to the maximum of the last timepoint or vice versa. This approach ensures the fastest possible slope in 95% of sampling. Permutation modeling entailed performing linear regression across time on a random 50 samples of either the full 520 (for RNAseq) or 322 (DNAm), bootstrapped 1000 times. To account for the high-variance of *in vivo* data which likely overestimates rescaling factors (i.e., the rate of change), we subsampled the top 10% of fastest slopes of the resulting distribution of which the median was used for the final rescaling factor for each gene/methylation site.

Statistical Analyses

All statistical analyses were performed using GraphPad Prism (v9.0) or RStudio (v1.3.1056) using R (v4.0.2). Comparisons of end of life to early life were performed using two-tailed paired ratio t-tests using the minimum and maximum values across lifespan. If no clear maximum or minimum value was present in the trajectory, then the average of the first or last three timepoints were used. Data visualization and statistical analyses were generated in R ('ggplot2', v3.3.5) and Prism 9.

Data Availability

All data can be accessed, visualized, and downloaded without restrictions at https://columbia-picard.shinyapps.io/shinyapp-Lifespan_Study/. All data visualized is downloadable as a .csv file which can further be found directly at: https://figshare.com/articles/dataset/Lifespan_Study_Data/18441998. The unprocessed RNAseq (GSE179848) and EPIC DNA methylation array data (GSE179847) can be accessed and downloaded in full through Gene Expression Omnibus (GEO). Brightfield microscopy images can be downloaded at: https://figshare.com/articles/dataset/Brightfield_Images_for_Cellular_Lifespan_Study/18444731.

Raw Seahorse assay files along with corresponding data analysis scripts can be found at : https://github.com/gav-sturm/Cellular_Lifespan_Study/tree/main/Seahorse. *In vivo* omics data can be found at their respective databases: GTEx RNAseq (dbGAP phs000424.v8.p2) and TwinsUK DNA methylation (GEO GSE90124). The R code for the computational pipeline used to estimate rescaling factors is further available at https://github.com/gav-sturm/Cellular_Lifespan_Study/tree/main/Rescaling.

Code Availability

Code is available at https://github.com/gav-sturm/Cellular_Lifespan_Study

Acknowledgments

This work was supported by NIH grant AG066828, the Wharton Fund, and the Baszucki Brain Research Fund to M.P. C.P.K. thanks the Charities Aid Foundation of Canada (CAF) for supporting this work. Special thanks to Wallace Marshall for his conceptual insights and mentorship while drafting this manuscript. The authors are grateful to Anna Monzel for insightful input on drafts of this manuscript, and to Michio Hirano for providing the SURF1 and control cell lines.

Author contributions

G.S. and M.P. designed the in vitro studies. G.S., performed cell culture and sample collection. G.S. and J.M. performed replication experiments. N.B performed inflection point analysis. G.S. and R.A.T. performed age-related statistical modeling. G.S. and C.K. performed all other data anlayses. C.K. developed theory for novel interpretation of the data. G.S., C.K., and M.P. drafted the manuscript. All authors reviewed and approved the final version of this manuscript.

Competing interests

The authors declare no competing interest.

Supplementary files

Supplemental File 1. Cell-to-whole body oxygen consumption calculator

Supplemental File 2. RNAseq gerenalized addivitive modeling significant age-related genes

Supplemental File 3. DNA methylation gerenalized addivitive modeling significant age-related CpGs

Supplemental File 4. ShinyGO gene set enriched KEGG pathways for UPregulated RNAseq genes

Supplemental File 5. ShinyGO gene set enriched KEGG pathways for DOWNregulated RNAseq genes

Supplemental File 6. ShinyGO gene set enriched Gene Ontology processes for UPregulated RNAseq genes

Supplemental File 7. ShinyGO gene set enriched Gene Ontology processes for DOWNregulated RNAseq genes

Supplemental File 8. Gene expression heatmaps of selected pathways across cellular lifespan

References

Bank, World. 2017. “Life Expectancy at Birth, Total (years)| Data.” https://data.worldbank.org/indicator/SP.DYN.LE00.IN?end=2018&start=1960&type=shaded&view=map.

Basisty, Nathan, Abhijit Kale, Ok Hee Jeon, Chisaka Kuehnemann, Therese Payne, Chirag Rao, Anja Holtz, et al. 2020. “A Proteomic Atlas of Senescence-Associated Secretomes for Aging Biomarker Development.” *PLoS Biology* 18 (1): e3000599.

Belmonte, Frances R., James L. Martin, Kristin Frescura, Joana Damas, Filipe Pereira, Mark A. Tarnopolsky, and Brett A. Kaufman. 2016. “Digital PCR Methods Improve Detection Sensitivity and Measurement Precision of Low Abundance mtDNA Deletions.” *Scientific Reports* 6 (April): 25186.

Belsky, Daniel W., Avshalom Caspi, Louise Arseneault, Andrea Baccarelli, David L. Corcoran, Xu Gao, Eiliss Hannon, et al. 2020. “Quantification of the Pace of Biological Aging in Humans through a Blood Test, the DunedinPoAm DNA Methylation Algorithm.” *eLife* 9 (May). https://doi.org/10.7554/eLife.54870.

Belsky, Daniel W., Avshalom Caspi, David L. Corcoran, Karen Sugden, Richie Poulton, Louise Arseneault, Andrea Baccarelli, et al. 2022. “DunedinPACE, a DNA Methylation Biomarker of the Pace of Aging.” *eLife* 11 (January). https://doi.org/10.7554/eLife.73420.

Bergen, Volker, Marius Lange, Stefan Peidli, F. Alexander Wolf, and Fabian J. Theis. 2020. “Generalizing RNA Velocity to Transient Cell States through Dynamical Modeling.” *Nature Biotechnology* 38 (12): 1408–14.

Bobba-Alves, Natalia, Gabriel Sturm, Jue Lin, Sarah A. Ware, Kalpita R. Karan, Anna Monzel, Céline Bris, et al. 2022. “Chronic Glucocorticoid Stress Reveals Increased Energy Expenditure and Accelerated Aging as Cellular Features of Allostatic Load.” *bioRxiv*. https://doi.org/10.1101/2022.02.22.481548.

Brand, Martin D., and David G. Nicholls. 2011. “Assessing Mitochondrial Dysfunction in Cells.” *Biochemical Journal* 435 (2): 297–312.

Bray, Nicolas L., Harold Pimentel, Páll Melsted, and Lior Pachter. 2016. “Erratum: Near-Optimal Probabilistic RNA-Seq Quantification.” *Nature Biotechnology* 34 (8): 888.

Brookes, Paul S., and Ana Gabriela Jimenez. 2021. “Metabolomics of Aging in Primary Fibroblasts from Small and Large Breed Dogs.” *GeroScience* 43 (4): 1683–96.

Brown, James H., James F. Gillooly, Andrew P. Allen, Van M. Savage, and Geoffrey B. West. 2004. “Toward a Metabolic Theory of Ecology.” *Ecology* 85 (7): 1771–89.

Brown, Thomas M., and Karthik Krishnamurthy. 2021. “Histology, Dermis.” In *StatPearls*. Treasure Island (FL): StatPearls Publishing.

Buttgereit, F., and M. D. Brand. 1995. “A Hierarchy of ATP-Consuming Processes in Mammalian Cells.” *Biochemical Journal* 312 (Pt 1) (November): 163–67.

Cagan, Alex, Adrian Baez-Ortega, Natalia Brzozowska, Federico Abascal, Tim H. H. Coorens, Mathijs A. Sanders, Andrew R. J. Lawson, et al. 2022. “Somatic Mutation Rates Scale with Lifespan across Mammals.” *Nature*, April. https://doi.org/10.1038/s41586-022-04618-z.

Campisi, J. 1997. “The Biology of Replicative Senescence.” *European Journal of Cancer* 33 (5): 703–9.

Careau, Vincent, Lewis G. Halsey, Herman Pontzer, Philip N. Ainslie, Lene F. Andersen, Liam J. Anderson, Lenore Arab, et al. 2021. “Energy Compensation and Adiposity in Humans.” *Current Biology: CB* 31 (20): 4659–66.e2.

Cawthon, Richard M. 2002. “Telomere Measurement by Quantitative PCR.” *Nucleic Acids Research* 30 (10): e47.

Chan, Michelle, Han Yuan, Ilya Soifer, Tobias M. Maile, Rebecca Y. Wang, Andrea Ireland, Jonathon J. O’Brien, et al. 2022. “Novel Insights from a Multiomics Dissection of the Hayflick Limit.” *eLife* 11 (February). https://doi.org/10.7554/eLife.70283.

Chrétien, Dominique, Paule Bénit, Hyung-Ho Ha, Susanne Keipert, Riyad El-Khoury, Young-Tae Chang, Martin Jastroch, Howard T. Jacobs, Pierre Rustin, and Malgorzata Rak. 2018. “Mitochondria Are Physiologically Maintained at close to 50 °C.” *PLOS Biology*. https://doi.org/10.1371/journal.pbio.2003992.

Coppé, Jean-Philippe, Pierre-Yves Desprez, Ana Krtolica, and Judith Campisi. 2010. “The Senescence-Associated Secretory Phenotype: The Dark Side of Tumor Suppression.” *Annual Review of Pathology* 5: 99–118.

Correia-Melo, Clara, Stephan Kamrad, Christoph B. Messner, Roland Tengölics, Lucía Herrera-Dominguez, St John Townsend, Mohammad Tauqeer Alam, et al. 2022. “Cell-Cell Metabolite Exchange Creates a pro-Survival Metabolic Environment That Extends Lifespan.” *bioRxiv*. https://doi.org/10.1101/2022.03.07.483228.

Correia-Melo, C., F. D. M. Marques, and R. Anderson. 2016. “Mitochondria Are Required for Pro-ageing Features of the Senescent Phenotype.” *The EMBO Journal*. http://emboj.embopress.org/content/35/7/724.abstract.

Davies, M. 1961. “On Body Size and Tissue Respiration.” *Journal of Cellular and Comparative Physiology* 57 (June): 135–47.

DeLong, John P., Jordan G. Okie, Melanie E. Moses, Richard M. Sibly, and James H. Brown. 2010. “Shifts in Metabolic Scaling, Production, and Efficiency across Major Evolutionary Transitions of Life.” *Proceedings of the National Academy of Sciences of the United States of America* 107 (29): 12941–45.

Demanelis, Kathryn, Farzana Jasmine, Lin S. Chen, Meytal Chernoff, Lin Tong, Dayana Delgado, Chenan Zhang, et al. 2020. “Determinants of Telomere Length across Human Tissues.” *Science*. https://doi.org/10.1126/science.aaz6876.

Economos, A. C. 1980. “Taxonomic Differences in the Mammalian Life Span-Body Weight Relationship and the Problem of Brain Weight.” *Gerontology* 26 (2): 90–98.

Ferrucci, Luigi, David M. Wilson, Stefano Donegà, and Myriam Gorospe. 2022. “The Energy–splicing Resilience Axis Hypothesis of Aging.” *Nature Aging*. https://doi.org/10.1038/s43587-022-00189-w.

Gavrilov, Leonid A., and Natalia S. Gavrilova. 2002. “Evolutionary Theories of Aging and Longevity.” *TheScientificWorldJournal* 2 (February): 339–56.

Grundberg, Elin, Eshwar Meduri, Johanna K. Sandling, Asa K. Hedman, Sarah Keildson, Alfonso Buil, Stephan Busche, et al. 2013. “Global Analysis of DNA Methylation Variation in Adipose Tissue from Twins Reveals Links to Disease-Associated Variants in Distal Regulatory Elements.” *American Journal of Human Genetics* 93 (5): 876–90.

Hannum, Gregory, Justin Guinney, Ling Zhao, Li Zhang, Guy Hughes, Srinivas Sadda, Brandy Klotzle, et al. 2013. “Genome-Wide Methylation Profiles Reveal Quantitative Views of Human Aging Rates.” *Molecular Cell* 49 (2): 359–67.

Hatton, Ian A., Andy P. Dobson, David Storch, Eric D. Galbraith, and Michel Loreau. 2019. “Linking Scaling Laws across Eukaryotes.” *Proceedings of the National Academy of Sciences of the United States of America* 116 (43): 21616–22.

Haugen, Thomas, Gøran Paulsen, Stephen Seiler, and Øyvind Sandbakk. 2018. “New Records in Human Power.” *International Journal of Sports Physiology and Performance* 13 (6): 678–86.

Hayflick, Leonard, and Paul S. Moorhead. 1964. “THE LIMITED IN VITRO LIFETIME OF HUMAN DIPLOID CELL STRAINS.” *Cytogenetics of Cells in Culture*. https://doi.org/10.1016/b978-1-4832-3075-7.50017-7.

Healy, Kevin, Luke McNally, Graeme D. Ruxton, Natalie Cooper, and Andrew L. Jackson. 2013. “Metabolic Rate and Body Size Are Linked with Perception of Temporal Information.” *Animal Behaviour* 86 (4): 685–96.

Higgins-Chen, Albert T., Kyra L. Thrush, Yunzhang Wang, Pei-Lun Kuo, Meng Wang, Christopher J. Minteer, Ann Zenobia Moore, et al. 2021. “A Computational Solution for

Bolstering Reliability of Epigenetic Clocks: Implications for Clinical Trials and Longitudinal Tracking." *bioRxiv*. https://doi.org/10.1101/2021.04.16.440205.

Horvath, Steve. 2013. "DNA Methylation Age of Human Tissues and Cell Types." *Genome Biology* 14 (10): R115.

Horvath, Steve, Junko Oshima, George M. Martin, Ake T. Lu, Austin Quach, Howard Cohen, Sarah Felton, et al. 2018. "Epigenetic Clock for Skin and Blood Cells Applied to Hutchinson Gilford Progeria Syndrome and Ex Vivo Studies." *Aging* 10 (7): 1758–75.

Horvath, Steve, and Kenneth Raj. 2018. "DNA Methylation-Based Biomarkers and the Epigenetic Clock Theory of Ageing." *Nature Reviews. Genetics* 19 (6): 371–84.

Hou, Chen. 2013. "The Energy Trade-off between Growth and Longevity." *Mechanisms of Ageing and Development* 134 (9): 373–80.

Jang, Cholsoon, Sheng Hui, Xianfeng Zeng, Alexis J. Cowan, Lin Wang, Li Chen, Raphael J. Morscher, et al. 2019. "Metabolite Exchange between Mammalian Organs Quantified in Pigs." *Cell Metabolism*. https://doi.org/10.1016/j.cmet.2019.06.002.

Jeppesen, Tina Dysgaard, Mette Cathrine Orngreen, Gerrit van Hall, Ronald G. Haller, and John Vissing. 2009. "Fat Metabolism during Exercise in Patients with Mitochondrial Disease." *Archives of Neurology* 66 (3): 365–70.

Jimenez, Ana Gabriela, Josh Winward, Ursula Beattie, and William Cipolli. 2018. "Cellular Metabolism and Oxidative Stress as a Possible Determinant for Longevity in Small Breed and Large Breed Dogs." *PloS One* 13 (4): e0195832.

Johnson, Adiv A., Maxim N. Shokhirev, Tony Wyss-Coray, and Benoit Lehallier. 2020. "Systematic Review and Analysis of Human Proteomics Aging Studies Unveils a Novel Proteomic Aging Clock and Identifies Key Processes That Change with Age." *Ageing Research Reviews* 60 (July): 101070.

Johnson, Kaitlyn E., Grant Howard, William Mo, Michael K. Strasser, Ernesto A. B. F. Lima, Sui Huang, and Amy Brock. 2019. "Cancer Cell Population Growth Kinetics at Low Densities Deviate from the Exponential Growth Model and Suggest an Allee Effect." *PLoS Biology* 17 (8): e3000399.

Jones, Owen R., Alexander Scheuerlein, Roberto Salguero-Gómez, Carlo Giovanni Camarda, Ralf Schaible, Brenda B. Casper, Johan P. Dahlgren, et al. 2014. "Diversity of Ageing across the Tree of Life." *Nature* 505 (7482): 169–73.

Jumpertz, Reiner, Robert L. Hanson, Maurice L. Sievers, Peter H. Bennett, Robert G. Nelson, and Jonathan Krakoff. 2011. "Higher Energy Expenditure in Humans Predicts Natural Mortality." *The Journal of Clinical Endocrinology and Metabolism* 96 (6): E972–76.

Kaminsky, Leonard A., Ross Arena, Jonathan Myers, James E. Peterman, Amanda R. Bonikowske, Matthew P. Harber, Jose R. Medina Inojosa, Carl J. Lavie, and Ray W. Squires. 2021. "Updated Reference Standards for Cardiorespiratory Fitness Measured with Cardiopulmonary Exercise Testing: Data from the Fitness Registry and the Importance of Exercise National Database (FRIEND)." In *Mayo Clinic Proceedings*. Elsevier. https://www.sciencedirect.com/science/article/pii/S0025619621006455.

Kempes, Christopher P., Peter M. van Bodegom, David Wolpert, Eric Libby, Jan Amend, and Tori Hoehler. 2017. "Drivers of Bacterial Maintenance and Minimal Energy Requirements." *Frontiers in Microbiology* 8 (January): 31.

Kempes, Christopher P., Stephanie Dutkiewicz, and Michael J. Follows. 2012. "Growth, Metabolic Partitioning, and the Size of Microorganisms." *Proceedings of the National Academy of Sciences of the United States of America* 109 (2): 495–500.

Kempes, Christopher P., M. A. R. Koehl, and Geoffrey B. West. 2019. "The Scales That Limit: The Physical Boundaries of Evolution." *Frontiers in Ecology and Evolution* 7: 242.

Kempes, Christopher P., Geoffrey B. West, and John W. Pepper. 2020. "Paradox Resolved: The Allometric Scaling of Cancer Risk across Species." *arXiv [q-bio.OT]*. arXiv. http://arxiv.org/abs/2011.11099.

Kempes, Christopher P., David Wolpert, Zachary Cohen, and Juan Pérez-Mercader. 2017. “The Thermodynamic Efficiency of Computations Made in Cells across the Range of Life.” *Philosophical Transactions. Series A, Mathematical, Physical, and Engineering Sciences* 375 (2109). https://doi.org/10.1098/rsta.2016.0343.

Kitazoe, Yasuhiro, Hirohisa Kishino, Kumpei Tanisawa, Keiko Udaka, and Masashi Tanaka. 2019. “Renormalized Basal Metabolic Rate Describes the Human Aging Process and Longevity.” *Aging Cell* 18 (4): e12968.

Kramer, Andrew M., Luděk Berec, and John M. Drake. 2018. “Editorial: Allee Effects in Ecology and Evolution.” *The Journal of Animal Ecology* 87 (1): 7–10.

Kuo, P-L, J. A. Schrack, M. D. Shardell, M. Levine, A. Z. Moore, Y. An, P. Elango, et al. 2020. “A Roadmap to Build a Phenotypic Metric of Ageing: Insights from the Baltimore Longitudinal Study of Aging.” *Journal of Internal Medicine* 287 (4): 373–94.

Kwon, So Mee, Seongki Min, Un-Woo Jeoun, Min Seok Sim, Gu Hyun Jung, Sun Mi Hong, Byul A. Jee, Hyun Goo Woo, Changhan Lee, and Gyesoon Yoon. 2021. “Global Spliceosome Activity Regulates Entry into Cellular Senescence.” *FASEB Journal: Official Publication of the Federation of American Societies for Experimental Biology* 35 (1): e21204.

Lan, Ganhui, Pablo Sartori, Silke Neumann, Victor Sourjik, and Yuhai Tu. 2012. “The Energy–speed–accuracy Trade-off in Sensory Adaptation.” *Nature Physics* 8 (5): 422–28.

Lareau, Liana F., and Steven E. Brenner. 2015. “Regulation of Splicing Factors by Alternative Splicing and NMD Is Conserved between Kingdoms yet Evolutionarily Flexible.” *Molecular Biology and Evolution* 32 (4): 1072–79.

Lengefeld, Jette, Chia-Wei Cheng, Pema Maretich, Marguerite Blair, Hannah Hagen, Melanie R. McReynolds, Emily Sullivan, et al. 2021. “Cell Size Is a Determinant of Stem Cell Potential during Aging.” *Science Advances* 7 (46): eabk0271.

Levine, Morgan E., Diana Leung, Christopher Minteer, and John Gonzalez. 2019. “A DNA Methylation Fingerprint of Cellular Senescence.” *bioRxiv*. https://doi.org/10.1101/674580.

Levine, Morgan E., Ake T. Lu, Austin Quach, Brian H. Chen, Themistocles L. Assimes, Stefania Bandinelli, Lifang Hou, et al. 2018. “An Epigenetic Biomarker of Aging for Lifespan and Healthspan.” *Aging* 10 (4): 573–91.

Levin, Michael. 2021. “Bioelectric Signaling: Reprogrammable Circuits Underlying Embryogenesis, Regeneration, and Cancer.” *Cell* 184 (8): 1971–89.

Lin, Jue, Elissa Epel, Joshua Cheon, Candyce Kroenke, Elizabeth Sinclair, Marty Bigos, Owen Wolkowitz, Synthia Mellon, and Elizabeth Blackburn. 2010. “Analyses and Comparisons of Telomerase Activity and Telomere Length in Human T and B Cells: Insights for Epidemiology of Telomere Maintenance.” *Journal of Immunological Methods* 352 (1-2): 71–80.

Ljubuncic, Predrag, and Abraham Z. Reznick. 2009. “The Evolutionary Theories of Aging Revisited--a Mini-Review.” *Gerontology* 55 (2): 205–16.

Lonsdale, John, Jeffrey Thomas, Mike Salvatore, Rebecca Phillips, Edmund Lo, Saboor Shad, Richard Hasz, et al. 2013. “The Genotype-Tissue Expression (GTEx) Project.” *Nature Genetics* 45 (6): 580–85.

López-Otín, Carlos, Maria A. Blasco, Linda Partridge, Manuel Serrano, and Guido Kroemer. 2013. “The Hallmarks of Aging.” *Cell* 153 (6): 1194–1217.

López-Otín, Carlos, Lorenzo Galluzzi, José M. P. Freije, Frank Madeo, and Guido Kroemer. 2016. “Metabolic Control of Longevity.” *Cell* 166 (4): 802–21.

Lu, Ake T., Austin Quach, James G. Wilson, Alex P. Reiner, Abraham Aviv, Kenneth Raj, Lifang Hou, et al. 2019. “DNA Methylation GrimAge Strongly Predicts Lifespan and Healthspan.” *Aging* 11 (2): 303–27.

Lu, Ake T., Anne Seeboth, Pei-Chien Tsai, Dianjianyi Sun, Austin Quach, Alex P. Reiner, Charles Kooperberg, et al. 2019. “DNA Methylation-Based Estimator of Telomere Length.” *Aging* 11 (16): 5895–5923.

Manno, Gioele La, Gioele La Manno, Ruslan Soldatov, Amit Zeisel, Emelie Braun, Hannah Hochgerner, Viktor Petukhov, et al. 2018. “RNA Velocity of Single Cells.” *Nature*. https://doi.org/10.1038/s41586-018-0414-6.

Masoro, Edward J., and Steven N. Austad. 2011. *Handbook of the Biology of Aging*. Elsevier.

Matsuda, Mitsuhiro, Hanako Hayashi, Jordi Garcia-Ojalvo, Kumiko Yoshioka-Kobayashi, Ryoichiro Kageyama, Yoshihiro Yamanaka, Makoto Ikeya, Junya Toguchida, Cantas Alev, and Miki Ebisuya. 2020. “Species-Specific Segmentation Clock Periods Are due to Differential Biochemical Reaction Speeds.” *Science* 369 (6510): 1450–55.

McEwen, Lisa M., Kieran J. O’Donnell, Megan G. McGill, Rachel D. Edgar, Meaghan J. Jones, Julia L. MacIsaac, David Tse Shen Lin, et al. 2020. “The PedBE Clock Accurately Estimates DNA Methylation Age in Pediatric Buccal Cells.” *Proceedings of the National Academy of Sciences of the United States of America* 117 (38): 23329–35.

Mitsui, Y., and E. L. Schneider. 1976. “Relationship between Cell Replication and Volume in Senescent Human Diploid Fibroblasts.” *Mechanisms of Ageing and Development* 5 (1): 45–56.

Mitteldorf, Joshua. 2010. “Evolutionary Origins of Aging.” In *The Future of Aging: Pathways to Human Life Extension*, edited by Gregory M. Fahy, Michael D. West, L. Stephen Coles, and Steven B. Harris, 87–126. Dordrecht: Springer Netherlands.

Moayyeri, Alireza, Christopher J. Hammond, Ana M. Valdes, and Timothy D. Spector. 2013. “Cohort Profile: TwinsUK and Healthy Ageing Twin Study.” *International Journal of Epidemiology* 42 (1): 76–85.

Mookerjee, Shona A., Akos A. Gerencser, David G. Nicholls, and Martin D. Brand. 2018. “Quantifying Intracellular Rates of Glycolytic and Oxidative ATP Production and Consumption Using Extracellular Flux Measurements.” *Journal of Biological Chemistry*. https://doi.org/10.1074/jbc.aac118.004855.

Morowitz, Harold. 1978. *Foundations of Bioenergetics*. Academic Press.

Moses, Melanie E., Chen Hou, William H. Woodruff, Geoffrey B. West, Jeffery C. Nekola, Wenyun Zuo, and James H. Brown. 2008. “Revisiting a Model of Ontogenetic Growth: Estimating Model Parameters from Theory and Data.” *The American Naturalist* 171 (5): 632–45.

Nespolo, Roberto F., Carlos Mejias, and Francisco Bozinovic. 2022. “Why Bears Hibernate? Redefining the Scaling Energetics of Hibernation.” *Proceedings. Biological Sciences / The Royal Society* 289 (1973): 20220456.

Neurohr, Gabriel E., Rachel L. Terry, Jette Lengefeld, Megan Bonney, Gregory P. Brittingham, Fabien Moretto, Teemu P. Miettinen, et al. 2019. “Excessive Cell Growth Causes Cytoplasm Dilution And Contributes to Senescence.” *Cell* 176 (5): 1083–97.e18.

Niebel, Bastian, Simeon Leupold, and Matthias Heinemann. 2019. “An Upper Limit on Gibbs Energy Dissipation Governs Cellular Metabolism.” *Nature Metabolism* 1 (1): 125–32.

Park, Kidong, Jaesung Jang, Daniel Irimia, Jennifer Sturgis, James Lee, J. Paul Robinson, Mehmet Toner, and Rashid Bashir. 2008. “‘Living Cantilever Arrays’ for Characterization of Mass of Single Live Cells in Fluids.” *Lab on a Chip* 8 (7): 1034–41.

Payea, Matthew J., Carlos Anerillas, Ravi Tharakan, and Myriam Gorospe. 2021. “Translational Control during Cellular Senescence.” *Molecular and Cellular Biology* 41 (2). https://doi.org/10.1128/MCB.00512-20.

Petr, Michael A., Irene Alfaras, Melissa Krawcyzk, Woei-Nan Bair, Sarah J. Mitchell, Christopher H. Morrell, Stephanie A. Studenski, et al. 2021. “A Cross-Sectional Study of Functional and Metabolic Changes during Aging through the Lifespan in Male Mice.” *eLife* 10 (April). https://doi.org/10.7554/eLife.62952.

Picard, M., J. Zhang, S. Hancock, O. Derbeneva, R. Golhar, P. Golik, S. O’Hearn, et al. 2014. “Progressive Increase in mtDNA 3243A>G Heteroplasmy Causes Abrupt Transcriptional Reprogramming.” *Proceedings of the National Academy of Sciences*.

https://doi.org/10.1073/pnas.1414028111.

Pinti, Marcello, Elisa Cevenini, Milena Nasi, Sara De Biasi, Stefano Salvioli, Daniela Monti, Stefania Benatti, et al. 2014. “Circulating Mitochondrial DNA Increases with Age and Is a Familiar Trait: Implications for ‘Inflamm-Aging.’” *European Journal of Immunology* 44 (5): 1552–62.

Pirt, S. J. 1965. “The Maintenance Energy of Bacteria in Growing Cultures.” *Proceedings of the Royal Society of London. Series B, Containing Papers of a Biological Character. Royal Society* 163 (991): 224–31.

Pontzer, Herman. 2018. “Energy Constraint as a Novel Mechanism Linking Exercise and Health.” *Physiology* 33 (6): 384–93.

Pontzer, Herman, Yosuke Yamada, Hiroyuki Sagayama, Philip N. Ainslie, Lene F. Andersen, Liam J. Anderson, Lenore Arab, et al. 2021. “Daily Energy Expenditure through the Human Life Course.” *Science* 373 (6556): 808–12.

Rando, Thomas A., and Tony Wyss-Coray. 2021. “Asynchronous, Contagious and Digital Aging.” *Nature Aging* 1 (1): 29–35.

Rising, Russell, Debora Duro, Maribel Cedillo, Sandra Valois, and Fima Lifshitz. 2003. “Daily Metabolic Rate in Healthy Infants.” *The Journal of Pediatrics* 143 (2): 180–85.

Rolfe, D. F., and G. C. Brown. 1997. “Cellular Energy Utilization and Molecular Origin of Standard Metabolic Rate in Mammals.” *Physiological Reviews* 77 (3): 731–58.

Ruggiero, Carmelinda, E. Jeffrey Metter, Vojtech Melenovsky, Antonio Cherubini, Samer S. Najjar, Alessandro Ble, Umberto Senin, Dan L. Longo, and Luigi Ferrucci. 2008. “High Basal Metabolic Rate Is a Risk Factor for Mortality: The Baltimore Longitudinal Study of Aging.” *The Journals of Gerontology. Series A, Biological Sciences and Medical Sciences* 63 (7): 698–706.

Savage, Van M., Andrew P. Allen, James H. Brown, James F. Gillooly, Alexander B. Herman, William H. Woodruff, and Geoffrey B. West. 2007. “Scaling of Number, Size, and Metabolic Rate of Cells with Body Size in Mammals.” *Proceedings of the National Academy of Sciences of the United States of America* 104 (11): 4718–23.

Sayed, Nazish, Yingxiang Huang, Khiem Nguyen, Zuzana Krejciova-Rajaniemi, Anissa P. Grawe, Tianxiang Gao, Robert Tibshirani, et al. 2021. “An Inflammatory Aging Clock (iAge) Based on Deep Learning Tracks Multimorbidity, Immunosenescence, Frailty and Cardiovascular Aging.” *Nature Aging* 1 (July): 598–615.

Schmidt, Cameron A., Kelsey H. Fisher-Wellman, and P. Darrell Neufer. 2021. “From OCR and ECAR to Energy: Perspectives on the Design and Interpretation of Bioenergetics Studies.” *The Journal of Biological Chemistry* 297 (4): 101140.

Schmidt-Nielsen, Knut, and Schmidt-Nielsen Knut. 1984. *Scaling: Why Is Animal Size So Important?* Cambridge University Press.

Schrack, Jennifer A., Nicolas D. Knuth, Eleanor M. Simonsick, and Luigi Ferrucci. 2014. “‘IDEAL’ Aging Is Associated with Lower Resting Metabolic Rate: The Baltimore Longitudinal Study of Aging.” *Journal of the American Geriatrics Society* 62 (4): 667–72.

Speakman, John R. 2005a. “Correlations between Physiology and Lifespan - Two Widely Ignored Problems with Comparative Studies.” *Aging Cell*. https://doi.org/10.1111/j.1474-9726.2005.00162.x.

———. 2005b. “Body Size, Energy Metabolism and Lifespan.” *The Journal of Experimental Biology* 208 (Pt 9): 1717–30.

Stroustrup, Nicholas, Winston E. Anthony, Zachary M. Nash, Vivek Gowda, Adam Gomez, Isaac F. López-Moyado, Javier Apfeld, and Walter Fontana. 2016. “The Temporal Scaling of Caenorhabditis Elegans Ageing.” *Nature* 530 (7588): 103–7.

Sturm, Gabriel, Andres Cardenas, Marie-Abèle Bind, Steve Horvath, Shuang Wang, Yunzhang Wang, Sara Hägg, Michio Hirano, and Martin Picard. 2019. “Human Aging DNA Methylation Signatures Are Conserved but Accelerated in Cultured Fibroblasts.” *Epigenetics: Official*

Journal of the DNA Methylation Society 14 (10): 961–76.

Sturm, Gabriel, Kalpita R. Karan, Anna Monzel, Balaji S. Santhanam, Tanja Taivassalo, Céline Bris, Sarah A. Duplaga, et al. 2021. "OxPhos Dysfunction Causes Hypermetabolism and Reduces Lifespan in Cells and in Patients with Mitochondrial Diseases." *bioRxiv*. https://doi.org/10.1101/2021.11.29.470428.

Sturm, Gabriel, Anna S. Monzel, Kalpita R. Karan, Jeremy Michelson, Sarah A. Ware, Andres Cardenas, Jue Lin, et al. 2021. "A Multi-Omics and Bioenergetics Longitudinal Aging Dataset in Primary Human Fibroblasts with Mitochondrial Perturbations." *bioRxiv*. https://doi.org/10.1101/2021.11.12.468448.

Swovick, Kyle, Denis Firsanov, Kevin A. Welle, Jennifer R. Hryhorenko, John P. Wise Sr, Craig George, Todd L. Sformo, Andrei Seluanov, Vera Gorbunova, and Sina Ghaemmaghami. 2021. "Interspecies Differences in Proteome Turnover Kinetics Are Correlated With Life Spans and Energetic Demands." *Molecular & Cellular Proteomics: MCP* 20 (January): 100041.

Taivassalo, Tanja, Tina Dysgaard Jensen, Nancy Kennaway, Salvatore DiMauro, John Vissing, and Ronald G. Haller. 2003. "The Spectrum of Exercise Tolerance in Mitochondrial Myopathies: A Study of 40 Patients." *Brain: A Journal of Neurology* 126 (Pt 2): 413–23.

Takauji, Yuki, Takumi Wada, Asuka Takeda, Ikuru Kudo, Kensuke Miki, Michihiko Fujii, and Dai Ayusawa. 2016. "Restriction of Protein Synthesis Abolishes Senescence Features at Cellular and Organismal Levels." *Scientific Reports* 6 (January): 18722.

Tanaka, Toshiko, Nathan Basisty, Giovanna Fantoni, Julián Candia, Ann Z. Moore, Angelique Biancotto, Birgit Schilling, Stefania Bandinelli, and Luigi Ferrucci. 2020. "Plasma Proteomic Biomarker Signature of Age Predicts Health and Life Span." *eLife* 9 (November). https://doi.org/10.7554/eLife.61073.

Tanaka, Toshiko, Angelique Biancotto, Ruin Moaddel, Ann Zenobia Moore, Marta Gonzalez-Freire, Miguel A. Aon, Julián Candia, et al. 2018. "Plasma Proteomic Signature of Age in Healthy Humans." *Aging Cell* 17 (5): e12799.

Tan, Bie, Hao Xiao, Fengna Li, Liming Zeng, and Yulong Yin. 2015. "The Profiles of Mitochondrial Respiration and Glycolysis Using Extracellular Flux Analysis in Porcine Enterocyte IPEC-J2." *Animal Nutrition (Zhongguo Xu Mu Shou Yi Xue Hui)* 1 (3): 239–43.

Tencerova, Michaela, Morten Frost, Florence Figeac, Tina Kamilla Nielsen, Dalia Ali, Jens-Jacob Lindegaard Lauterlein, Thomas Levin Andersen, et al. 2019. "Obesity-Associated Hypermetabolism and Accelerated Senescence of Bone Marrow Stromal Stem Cells Suggest a Potential Mechanism for Bone Fragility." *Cell Reports* 27 (7): 2050–62.e6.

Trumpff, Caroline, Anna L. Marsland, Carla Basualto-Alarcón, James L. Martin, Judith E. Carroll, Gabriel Sturm, Amy E. Vincent, et al. 2019. "Acute Psychological Stress Increases Serum Circulating Cell-Free Mitochondrial DNA." *Psychoneuroendocrinology* 106 (August): 268–76.

Tumasian, Robert A., 3rd, Abhinav Harish, Gautam Kundu, Jen-Hao Yang, Ceereena Ubaida-Mohien, Marta Gonzalez-Freire, Mary Kaileh, et al. 2021. "Skeletal Muscle Transcriptome in Healthy Aging." *Nature Communications* 12 (1): 2014.

Ubaida-Mohien, Ceereena, Alexey Lyashkov, Marta Gonzalez-Freire, Ravi Tharakan, Michelle Shardell, Ruin Moaddel, Richard D. Semba, et al. 2019. "Discovery Proteomics in Aging Human Skeletal Muscle Finds Change in Spliceosome, Immunity, Proteostasis and Mitochondria." *eLife* 8 (October). https://doi.org/10.7554/eLife.49874.

Wang, Zimian, Zhiliang Ying, Anja Bosy-Westphal, Junyi Zhang, Britta Schautz, Wiebke Later, Steven B. Heymsfield, and Manfred J. Müller. 2010. "Specific Metabolic Rates of Major Organs and Tissues across Adulthood: Evaluation by Mechanistic Model of Resting Energy Expenditure." *The American Journal of Clinical Nutrition* 92 (6): 1369–77.

Ware, Sarah A., Nikita Desai, Mabel Lopez, Daniel Leach, Yingze Zhang, Luca Giordano, Mehdi

Nouraie, Martin Picard, and Brett A. Kaufman. 2020. “An Automated, High-Throughput Methodology Optimized for Quantitative Cell-Free Mitochondrial and Nuclear DNA Isolation from Plasma.” *The Journal of Biological Chemistry* 295 (46): 15677–91.

West, G. B., J. H. Brown, and B. J. Enquist. 1997. “A General Model for the Origin of Allometric Scaling Laws in Biology.” *Science* 276 (5309): 122–26.

———. 2001. “A General Model for Ontogenetic Growth.” *Nature* 413 (6856): 628–31.

West, Geoffrey. 2018. *Scale: The Universal Laws of Life, Growth, and Death in Organisms, Cities, and Companies*. Penguin.

West, Geoffrey B., James H. Brown, and Brian J. Enquist. 1999. “A General Model for the Structure and Allometry of Plant Vascular Systems.” *Nature* 400 (6745): 664–67.

West, Geoffrey B., William H. Woodruff, and James H. Brown. 2002. “Allometric Scaling of Metabolic Rate from Molecules and Mitochondria to Cells and Mammals.” *Proceedings of the National Academy of Sciences of the United States of America* 99 Suppl 1 (February): 2473–78.

Whittemore, Kurt, Elsa Vera, Eva Martínez-Nevado, Carola Sanpera, and Maria A. Blasco. 2019. “Telomere Shortening Rate Predicts Species Life Span.” *Proceedings of the National Academy of Sciences of the United States of America* 116 (30): 15122–27.

Wiley, Christopher D., and Judith Campisi. 2021. “The Metabolic Roots of Senescence: Mechanisms and Opportunities for Intervention.” *Nature Metabolism* 3 (10): 1290–1301.

Yang, Xingbo, Matthias Heinemann, Jonathon Howard, Greg Huber, Srividya Iyer-Biswas, Guillaume Le Treut, Michael Lynch, et al. 2021. “Physical Bioenergetics: Energy Fluxes, Budgets, and Constraints in Cells.” *Proceedings of the National Academy of Sciences of the United States of America* 118 (26). https://doi.org/10.1073/pnas.2026786118.

Yeakel, Justin D., Christopher P. Kempes, and Sidney Redner. 2018. “Dynamics of Starvation and Recovery Predict Extinction Risk and Both Damuth’s Law and Cope's Rule.” *Nature Communications* 9 (1): 657.

Youn, Ahrim, and Shuang Wang. 2018. “The MiAge Calculator: A DNA Methylation-Based Mitotic Age Calculator of Human Tissue Types.” *Epigenetics: Official Journal of the DNA Methylation Society* 13 (2): 192–206.

Zhao, Zhijun, Jing Cao, Chaoqun Niu, Menghuan Bao, Jiaqi Xu, Daliang Huo, Shasha Liao, Wei Liu, and John R. Speakman. 2022. “Body Temperature Is a More Important Modulator of Lifespan than Metabolic Rate in Two Small Mammals.” *Nature Metabolism*, March. https://doi.org/10.1038/s42255-022-00545-5.

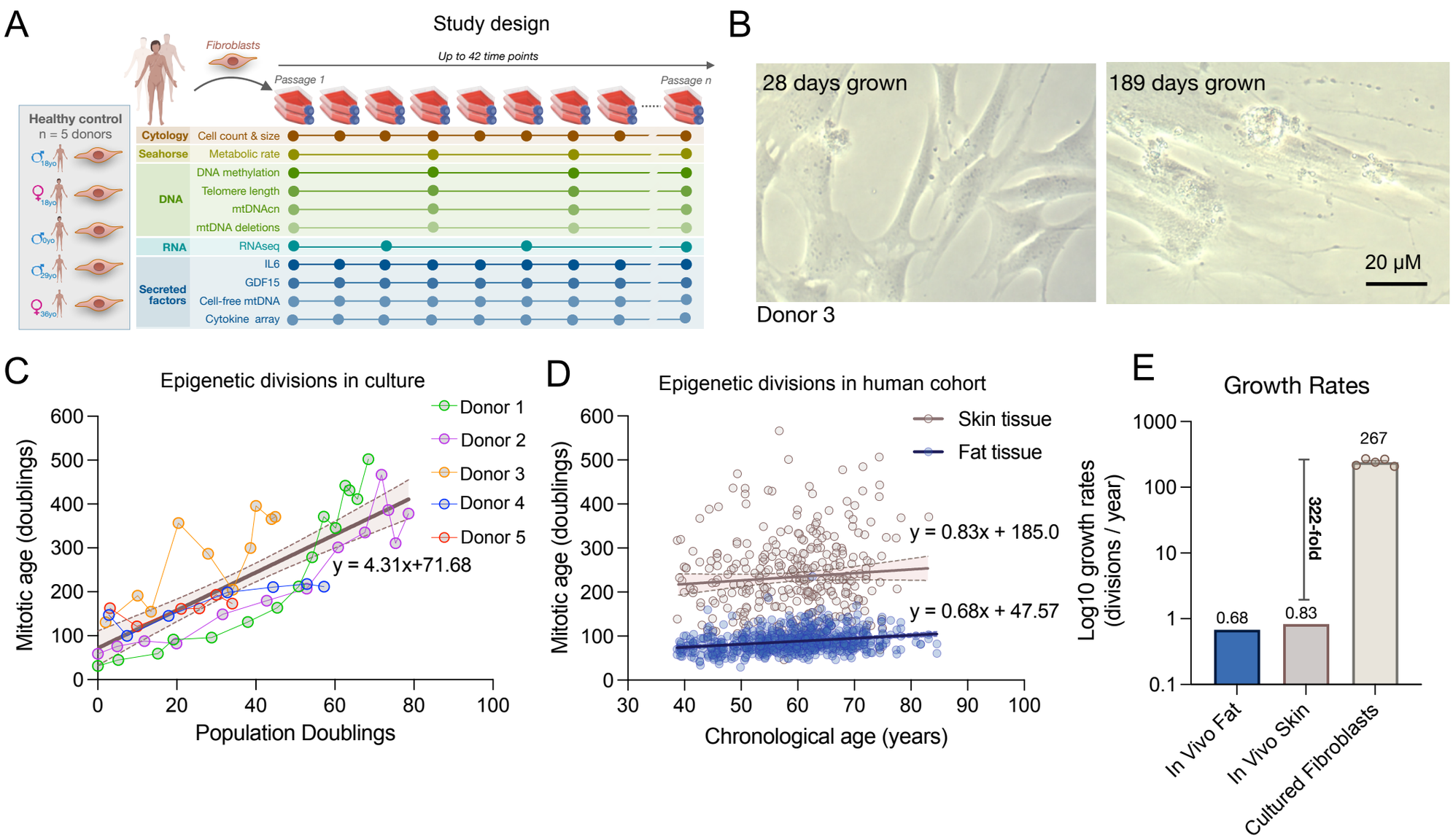

Extended Data Figure 1. Study design and growth rates of human fibroblasts. (**A**) Schematic of Cellular Lifespan Study design showing repeat measures collected as cells are passaged until replicative exhaustion. (**B**) Bright-field images of Donor 5 fibroblasts as young (left panel) and aged (right panel) morphology. Note how young cells have a spindle shapes that align side-by-side , while aged cells flatten with spider web-like protrusions. (**C**) Epigenetic-derived cellular divisions (Mitotic age) as a function of empirically measured division in cultured fibroblasts (n=51 timepoints across 5 donor lines). Fit line represents linear regression with 95% confidence intervals across all timepoints. (**D**) Mitotic age measured in fat (n=648) and skin (n=322) tissue samples across a population of aging female twins (TwinsUK study). Fit line represents linear regression with 95% confidence intervals for each tissue. (**E**) Derived growth rate for *in vivo* fat and skin tissue compared to cultured fibroblasts. Rates are expressed as log 10 cellular divisions per year.

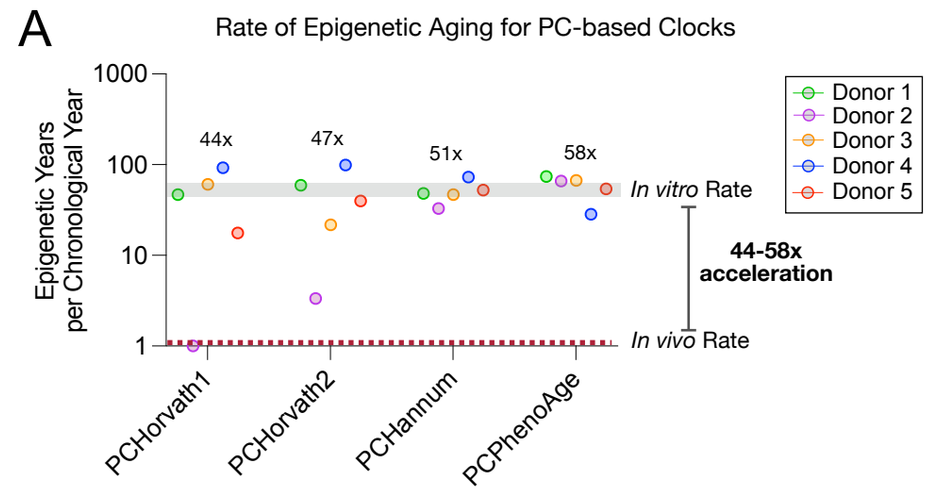

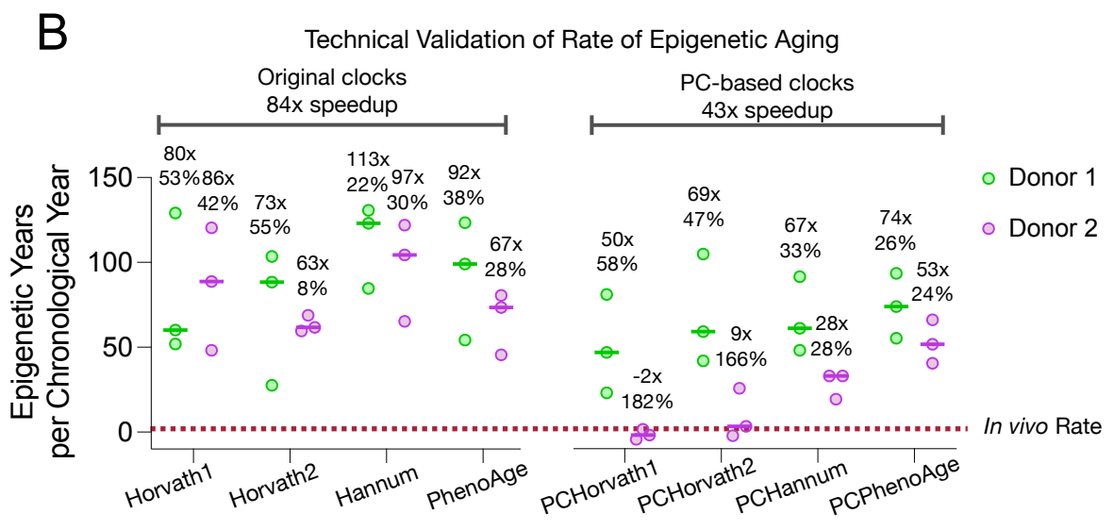

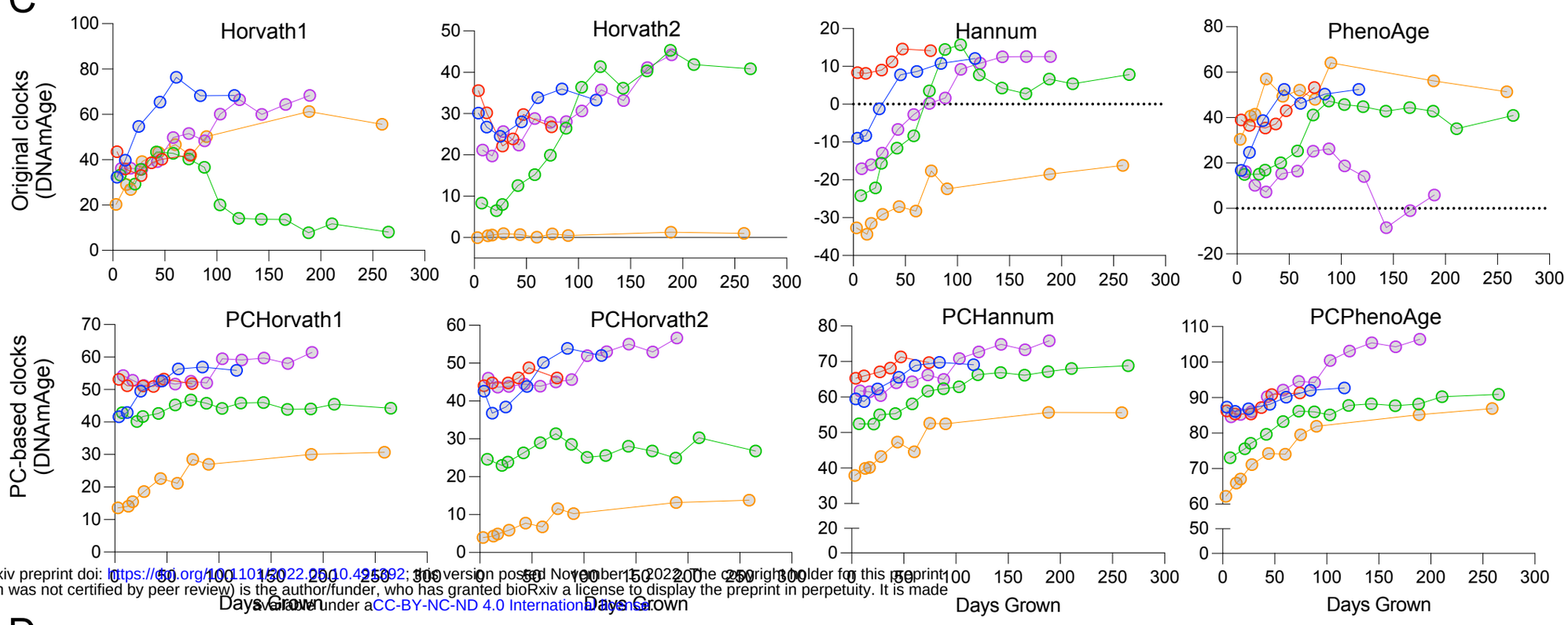

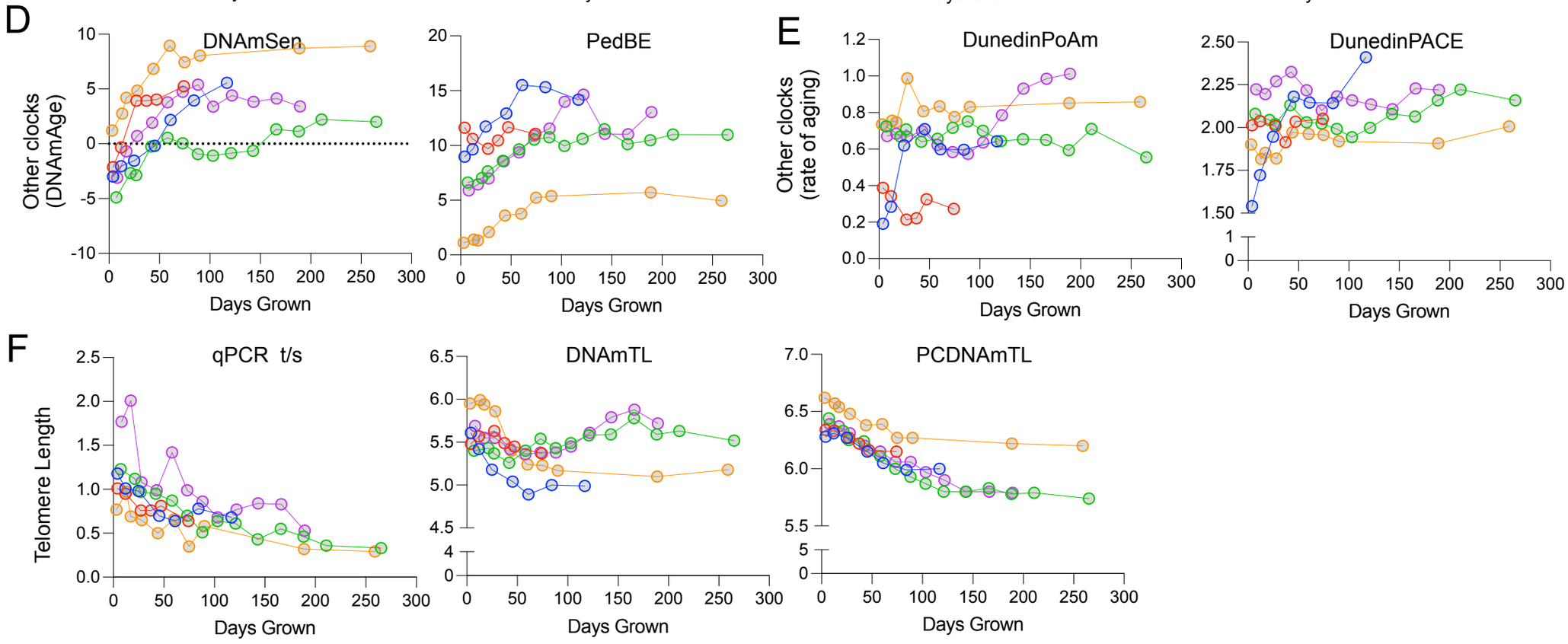

Extended Data Figure 2. Rate of epigenetic aging of cultured fibroblasts. (**A**) Rate of epigenetic aging for cultured fibroblasts as measured by several PC-based epigenetic clocks. Rates are defined as the slope of the linear fit line from days 10-70 of growth in culture. Red line indicates the *in vivo* rate of epigenetic aging of 1 biological year per a chronological year. (**B**) Repeat experiments measuring the variability in the rate of epigenetic aging for Donor 3 (male, green) and 4 (female, purple). N = 3 repeat experiments. Horizontal bar represents the mean of the rates, noted with average speed up and coefficient of variation per group. (**C**) DNAmAge over cellular lifespan for each original clock (top-panel) and PC-based clock (bottom-panel). Horvath1 i.e. PantTissue clock, Horvath2 i.e. Skin&Blood clock. (**D**) Other DNAmAge clocks specialized for cultured cells. (**E**) Dunedin clocks used as blood biomarker for the pace of aging. (**F**) Telomere length estimates using qPCR-based T/S ratio (left-panel), DNAmTL (middle-panel), and PC-based DNAmTL (right-panel).

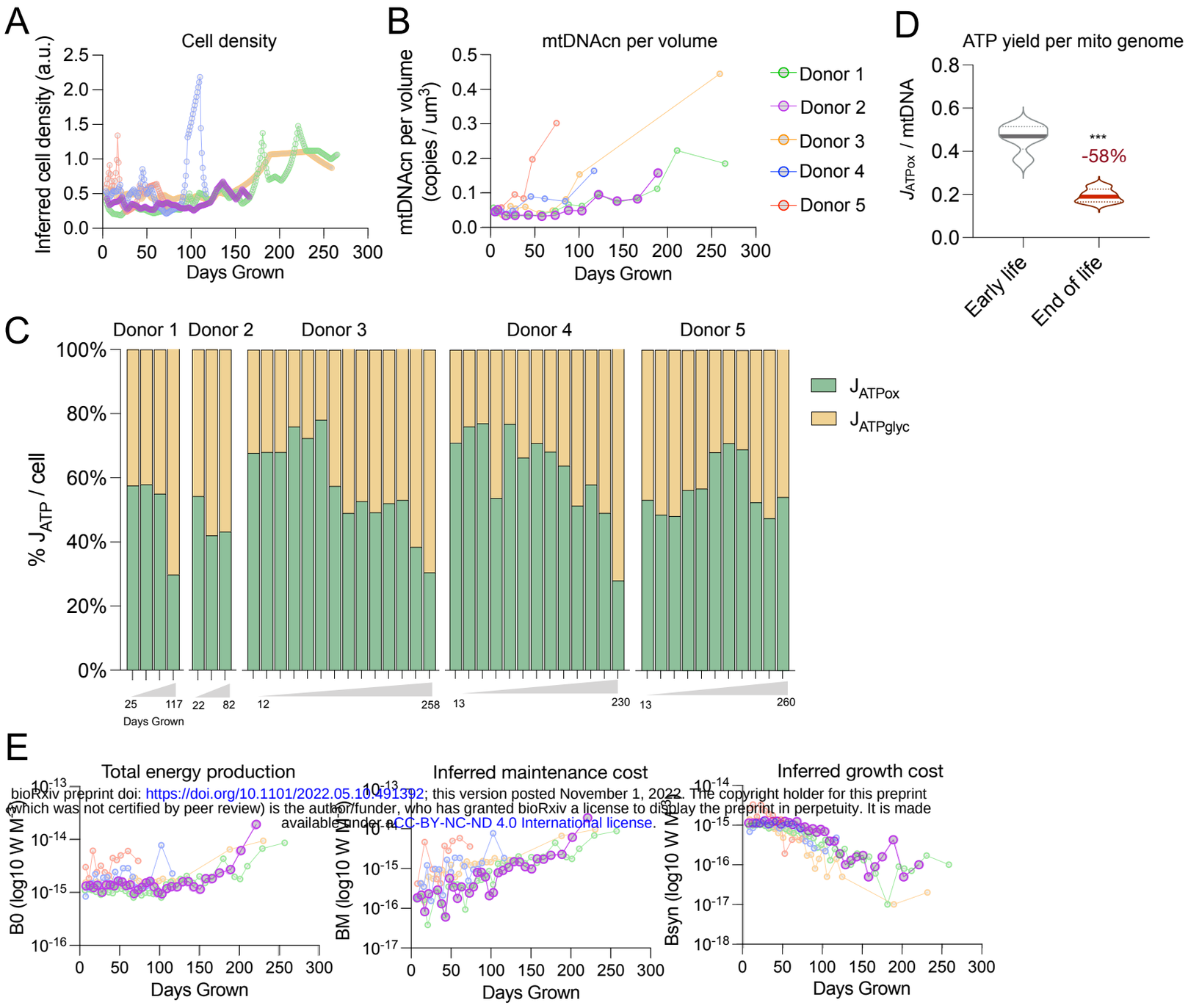

Extended Data Figure 3. Age-related shifts in cellular density and metabolic rates. (**A**) Indirect measure of cell density across cellular lifespan. Values are determined as the weighted sum of DNA, RNA, and protein mass per cell at a given timepoint. (**B**) Mitochondrial DNA per unit volume across the cellular lifespan. (**C**) Stacked barplot showing % of the rate of ATP production derived from OxPhos (J_{ATPox}, green) and ATP derived from glycolysis ($J_{ATPglyc}$, yellow). Blue triangle on x-axis indicates the age of the cells in days grown (increasing left-to-right). (**D**) Energetic efficiency of young and aged cells, measured as the ATP yield per a mitochondrial genome. Paired t-test, Hedge's G. (**E**) Inferred total energy production (B0, left-panel), maintenance costs (middle-panel), and growth costs (right-panel) across the cellular lifespan (see Box 1.II for derivation).

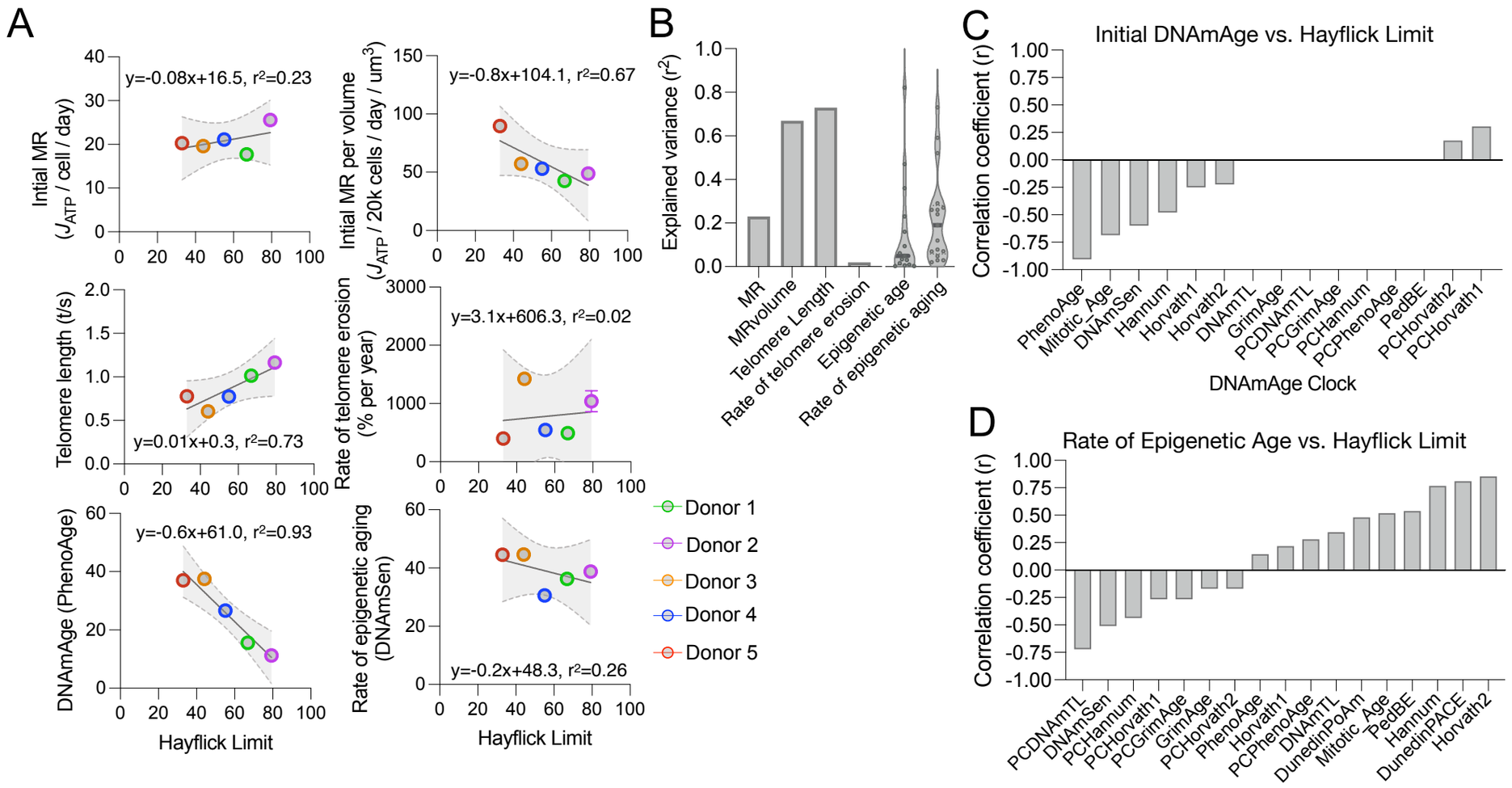

Extended Data Figure 4. Prediction of hayflick limit from MR and aging measures. (**A**) Correlation of hayflick limit (n=5 cell lines with metabolic rate; per cell (top-left) and per cell volume (top-right) (10-70days, 2-5 timepoints/cell line), telomere length; initial y-intercept (middle-left), rate of telomere length (middle-right) (10-70days, 4 timepoints/cell line), DNAmAge; initial y-intercept (bottom-left), and rate of epigenetic aging (bottom-right) (10-70days, 4-5 timepoints/cell line) (**B**) Explained variance in hayflick for each parameter. Epigenetic age and rate values are shown as a violin plot with each point indicating a different DNAmAge clock. (**C**) Correlation coefficient for each DNAmAge clock initial epigenetic age (y-intercept 10-70 days grown, 4-5 timepoints/cell line) with hayflick limit (n=5 cell lines). (**D**) Correlation coefficient for each clock's rate of epigenetic aging (slope, 10-70 days grown, 4-5 timepoints/cell line) with hayflick limit (n=5 cell lines). Note, Dunedin clocks are measures of the rate of aging and therefore were calculated using the mean of each donor for selected timepoints (10-70 days grown, 4-5 timepoints/cell line).

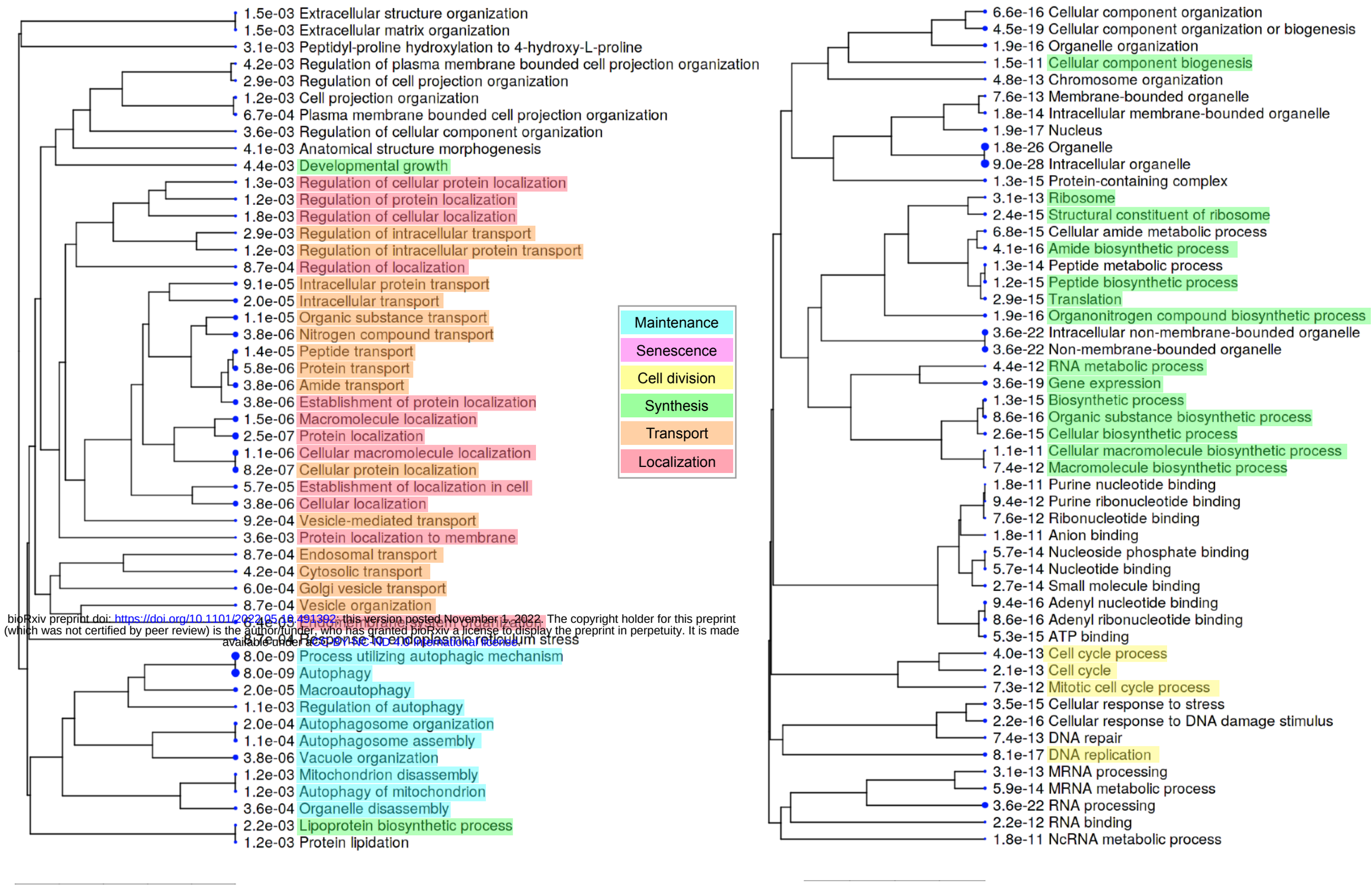

Extended Data Figure 5. Gene set enrichment of age-related gene expression. (**A**) Hierarchal clustering of enriched Gene Ontology pathways of age-related genes identified with generalized additive modeling. Highlighted processes are categorized by shared biological function. Only top 50 processes shown (see Supplemental Files 6 & 7 for full list).

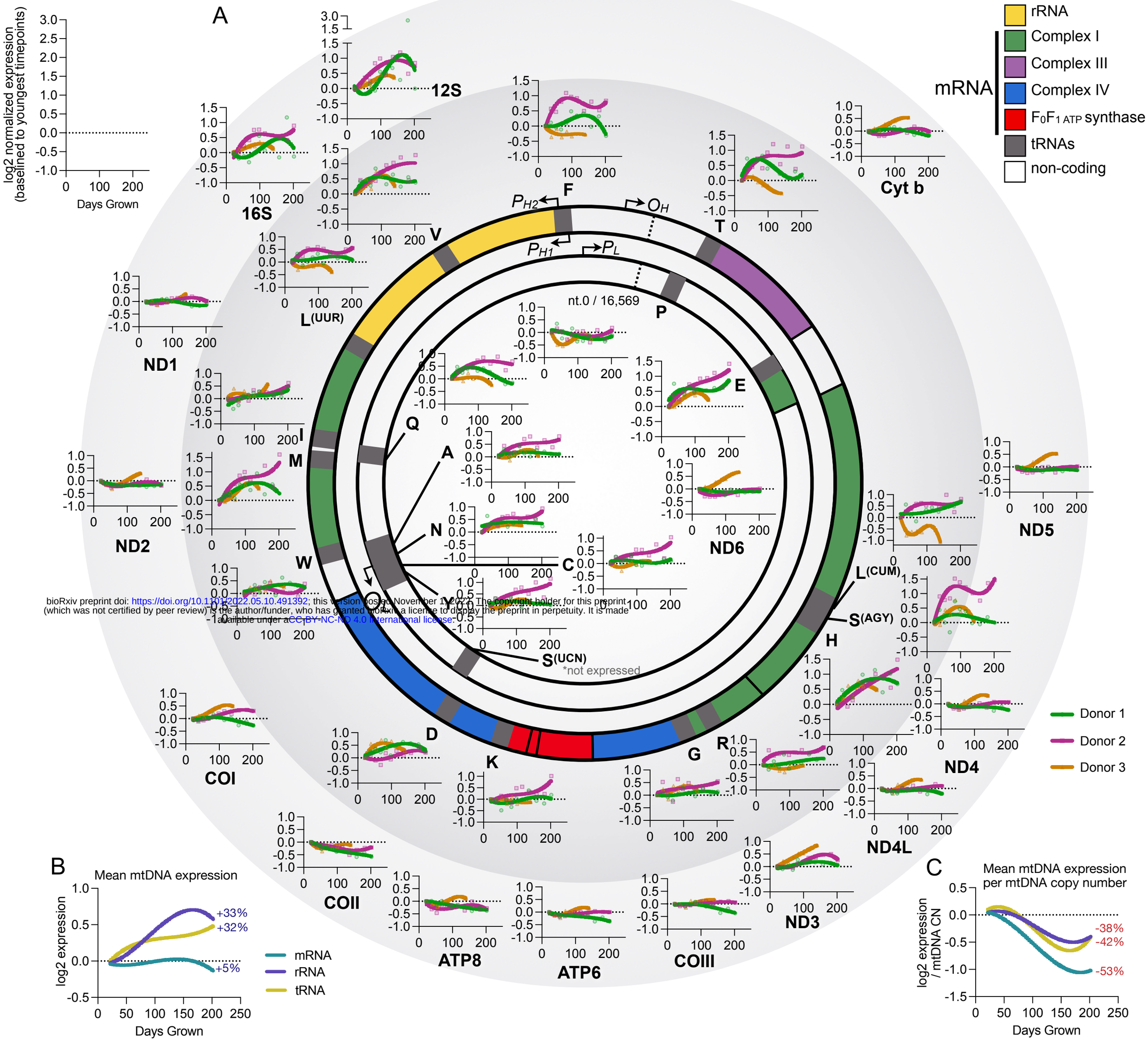

Extended Data Figure 6. mtDNA gene expression of coding genes and tRNAs. Circular mtDNA map with its 37 genes annotated. Graphs show normalized expression values (log2 fold-change relative to median of youngest timepoints) for 3 healthy donors across the cellular lifespan. The inner ring induces all transfer RNAs (tRNAs); the outer ring includes ribosomal and messenger RNA (rRNA and mRNA) genes. Graph height is scaled to the min/max of a given RNA. (**B**) Mean RNA species expression across the cellular lifespan. Values are the mean of log2 normalized expression baselined to youngest timepoints for the different RNA species (mRNA n=13, rRNA n=2, tRNA=22 genes). (**B**) Mean RNA species expression normalized to mtDNA copy number across the cellular lifespan. Copy number values are interpolated to match expression timepoints using generalized additive modeling (k=6).

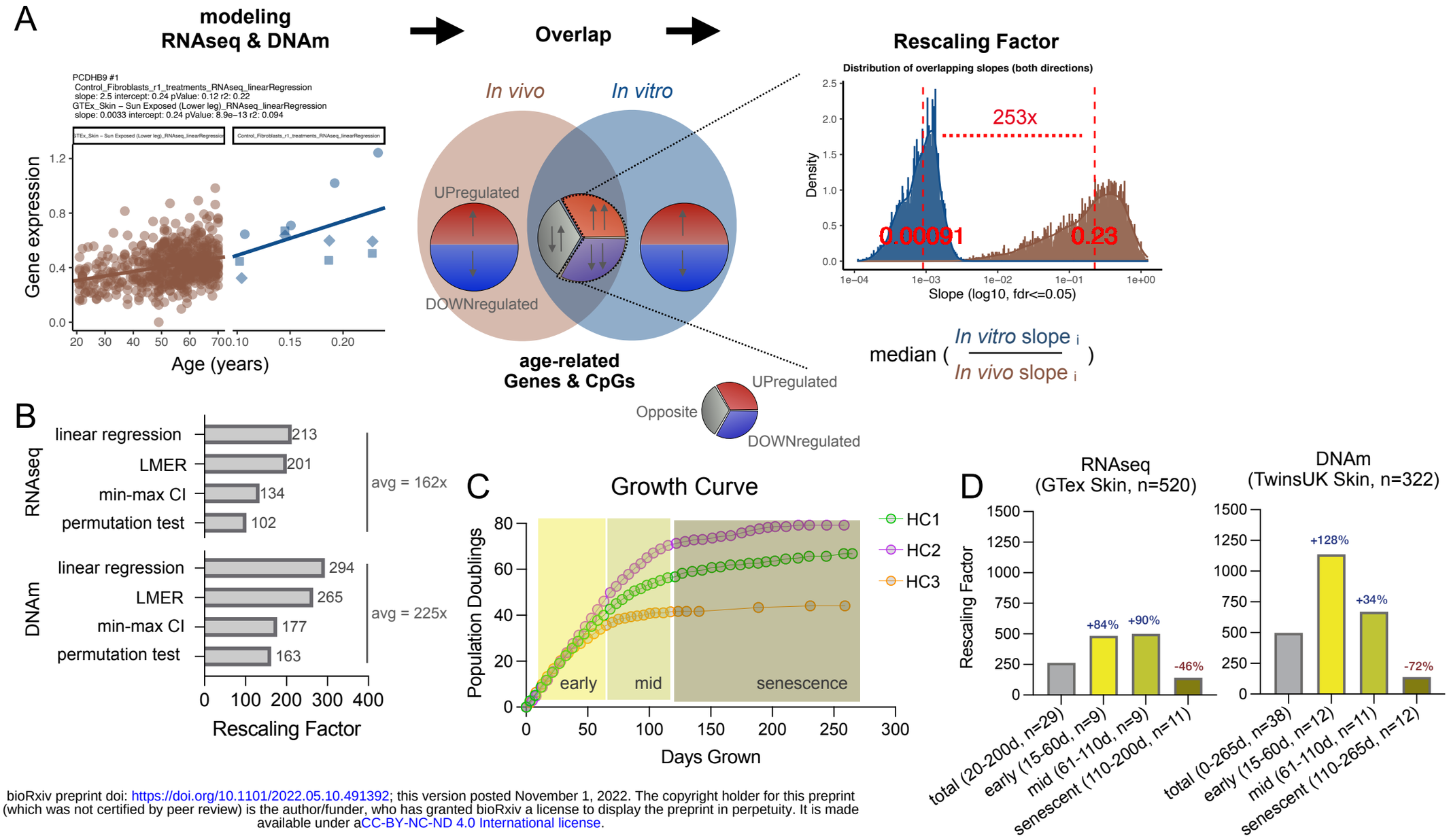

Extended Data Figure 7. Derivation of methylation and transcription rescaling factor between *in vivo* to *in vitro* systems. (**A**) Computational pipeline for deriving rescaling factors: Age-related gene expression and DNA methylation markers are selected from a linear modeling across lifespan in both *in vivo* and *in vitro* datasets. Genes and DNAm sites are than grouped by their direction of a change with age (UP or DOWN) and then the overlap of shared directional genes between the *in vivo* and *in vitro* datasets are selected. Finally, the rescaling factor is calculated as the ratio of the median *in vitro slopes* to the median of the *in vivo* slopes. (**B**) Rescaling factor based on different modeling techniques of the *in vivo* data. Note, all *in vitro* slopes were obtained using a linear model. (**C**) Growth curves of three untreated cell lines (Donor3-5). Color blocks indicate sections of lifespan operationalized as linear, mid, and senescent growth phases. (**D**) Comparison of rescaling factor depending on the portion of the cellular lifespan at which the slope was calculated. Genes and DNAm marker were selected from the same set of age-related molecules as identified by a full-lifespan nonlinear generalized additive modeling (GAM).

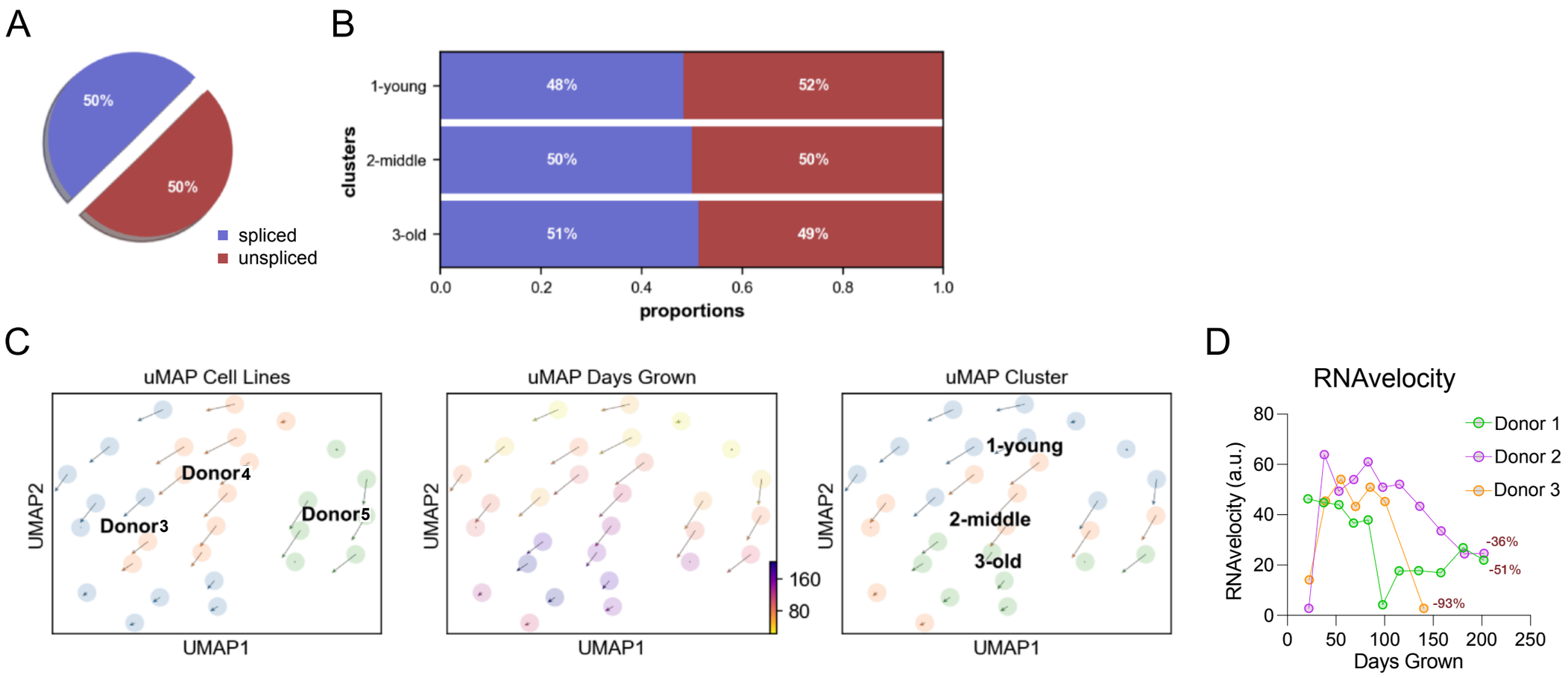

Extended Data Figure 8. RNAvelocity across cellular lifespan. (**A-D**) Rate of transcriptional events calculated as using ratios of splice : unspliced mRNA as outlined in La Manno et al. (REF. Nature, 2018) (**A**) Pi chart of number of splice to unspliced mRNA. (**B**) Splice ratio grouped by age of cells. Young = 0-60 days, middle = 61-110 days, old = 110-200 days. (**C**) Uniform manifold approximation and projection (uMAP) applied for dimension reduction of gene expression data shown by donor (left-panel), days grown (middle-panel) and clustered age group (right-panel). Length of arrows at each point indicate the RNAvelocity measured using stochastic modeling. (**D**) RNAvelocity rates across cellular lifespan confirming the slow-down of transcriptional events as cells age *in vitro.* Percent values are the final timepoint / average of the first three timepoints.

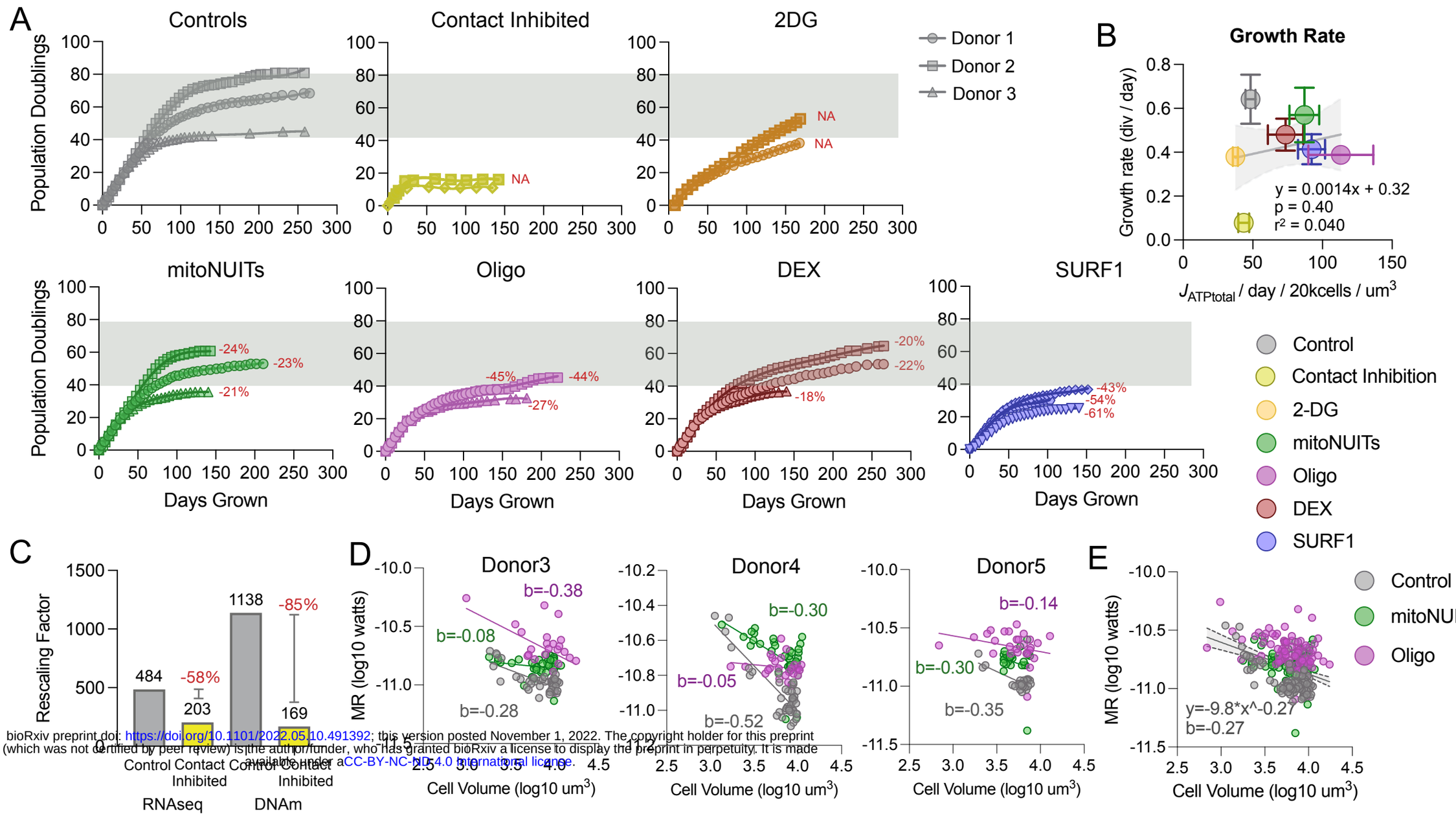

Extended Data Figure 9. Alteration of metabolic rate with pharmacological, genetic, and environmental perturbations. (**A**) Growth curves of each perturbation. Gray bar indicated range of the hayflick limit for untreated controls. 2-3 donors per condition. 2DG had limited growth curve due to experimental artifact. (**B**) Growth rate for each perturbation correlated with MR per volume. Growth rates are calculated between 15-60 days of growth. Gray line indicates linear regression with faded gray region indicated range of error. (**C**) Rescaling factor deceleration from contact inhibition for RNAseq and DNA methylation data. (**D-E**) Allometric scaling of cell volume to metabolic rate (MR) for selected treatment groups (controls, mitoNUITs, oligo) with time matched sampling. Treatments were selected to ensure matching timepoints across lifespan. Scaling coefficient for each cell line (D) and as for all aggregated data (E). B value indicates metabolic scaling coefficient which is -0.25 across species.

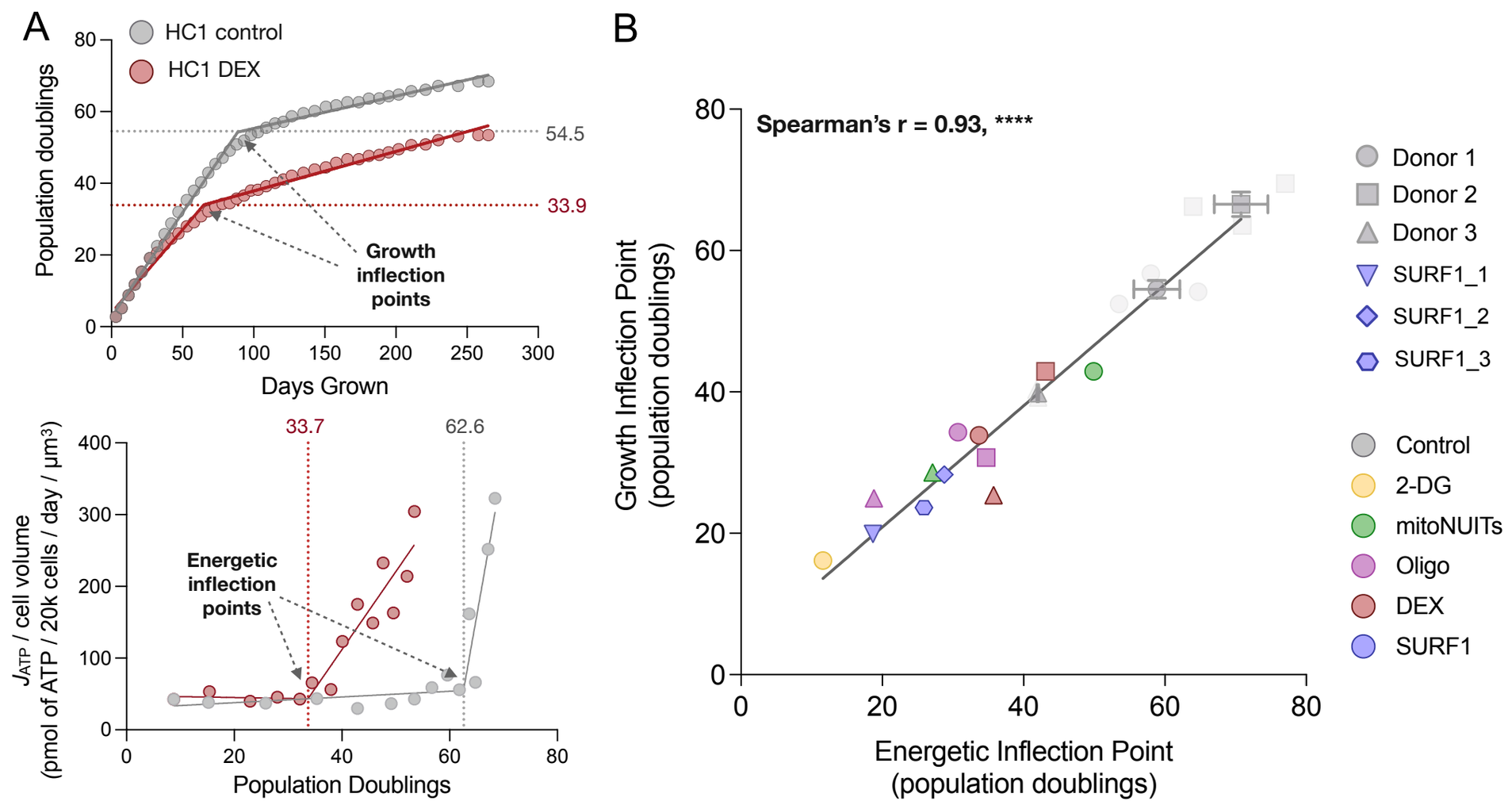

Extended Data Figure 10. Inflection point analysis of energetic and growth curves. (**A**) Example analysis pipeline to derive energetic and growth inflection points (healthy control 1 untreated and 100nM dexamethasone shown). Inflection points were derived using the X0 value of a two-segment linear regression. (**B**) Linear correlation between the number of doublings underwent at the energetic and growth inflection points. Error bars indicate S.E.M. across 2-3 replicate lifespan experiments and were only performed on untreated cell lines. Faded gray points are 2-3 replicate experiments of untreated cells (only mean value included in correlation). R value indicates spearman correlation. **** $p < 0.0001$.

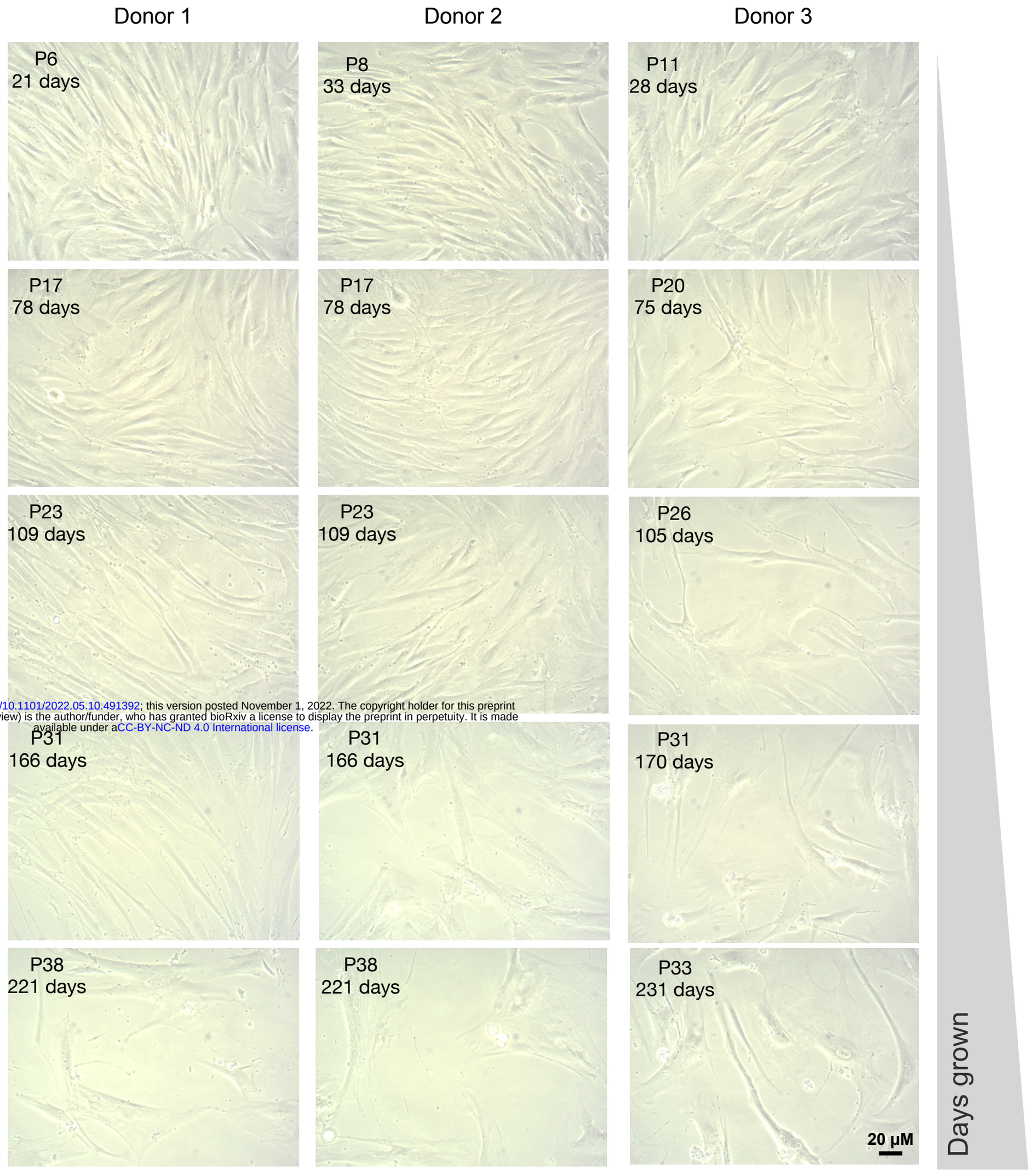

Extended Data Figure 11. Bright-field microscopy images of fibroblasts across replicative lifespan. Phase contrast bright field images of cultured fibroblasts across cellular lifespan. Images were taken with a 20k objective after 5-7 days of growth.